AN ABSTRACT OF THE THESIS OF

Tanarat Potisuk for the degree of Master of Science in Civil Engineering presented on July 24, 2000.

Title: Finite Element Modeling of Reinforced Concrete Beams Externally Strengthened by FRP Composites.

Abstract approved: Redacted for privacy

Damian I. Kachlakev, Thomas H. Miller

Three-dimensional finite element models are developed to simulate the behavior of four full-scale reinforced concrete beams. The beams are constructed with different fiber-reinforced polymer (FRP) strengthening schemes, and are modeled using ANSYS, a commercially available finite element analysis program. The experimental beams replicate the transverse beams of the Horsetail Creek Bridge, and were constructed and tested at Oregon State University. The finite element models use a smeared cracking approach for the concrete and three-dimensional layered elements to model the FRP composites.

It was found that the finite element models could effectively simulate the behavior of the full-scale beams. Results obtained from the finite element analysis are presented and compared with the experimental data from the full-scale beam tests through the linear and nonlinear ranges up to failure. Comparisons are made for load-strain plots, load-deflection plots, first cracking loads, loads at failure, and crack

patterns at failure. The results from the finite element analysis show good agreement with those from the experimental data and support hand calculation predictions for the experiment very well. The crack patterns at failure predicted by the finite element program strongly corroborate the failure modes observed for the full-scale beam tests. Recommendations for finite element modeling improvement are included.

© Copyright by Tanarat Potisuk
July 24, 2000
All Rights Reserved

Finite Element Modeling of Reinforced Concrete Beams Externally Strengthened by FRP Composites

by

Tanarat Potisuk

A THESIS

Submitted to

Oregon State University

In Partial Fulfillment of
the requirements for the
degree of

Master of Science

Presented July 24, 2000
Commencement June 2001

Master of Science thesis of Tanarat Potisuk presented on July 24, 2000

APPROVED:

Redacted for privacy

Co-Major Professor, representing Civil Engineering

Redacted for privacy

Co-Major Professor, representing Civil Engineering

Redacted for privacy

Head of Department of Civil, Construction, and Environmental Engineering

Redacted for privacy

Dean of Graduate School

I understand that my thesis will become part of the permanent collection of Oregon State University libraries. My signature below authorizes release of my thesis to any reader upon request.

Redacted for privacy

Tanarat Potisuk, Author

APPROVED:

Redacted for privacy

Committee Member, representing Civil Engineering

ACKNOWLEDGMENTS

I would like to express my appreciation to Dr. Damian I. Kachlakev, Dr. Thomas H. Miller, Dr. Solomon C. S. Yim, and Dr. Timothy C. Kennedy for their guidance, support, and assistance throughout this project. Thanks are also due to Dr. James R. Lundy for the valuable advice during the conduct of this thesis.

The financial support of the Oregon Department of Transportation and Department of Civil, Construction, and Environmental Engineering, Oregon State University, are appreciated. Special thanks go to my friends for their assistance during the conduct of this work. Finally, my gratitude also goes to my parents, Luechai and Naree Potisuk, for their encouragement, and my sisters and brother for their help.

TABLE OF CONTENTS

TABLE OF CONTENTS (Continued)

LIST OF FIGURES

LIST OF FIGURES (Continued)

LIST OF FIGURES (Continued)

LIST OF TABLES

LIST OF ATTACHMENTS

DISK A: Input Files

Folder: Control beam
Controlbeam (Geometric configurations and initial loading)
Loading(cont)
Postprocessing (Commands to obtain results)

Folder: Flexural beam
Flexbeam (Geometric configurations and initial loading)
Loading(cont)
Postprocessing (Commands to obtain results)

Folder: Shear beam
Shearbeam (Geometric configurations and initial loading)
Loading(cont)
Postprocessing (Commands to obtain results)

Folder: Flex_Shear beam
Flex_Shearbeam (Geometric configurations and initial loading)
Loading(cont)
Postprocessing (Commands to obtain results)

FINITE ELEMENT MODELING OF REINFORCED CONCRETE BEAMS EXTERNALLY STRENGTHENED BY FRP COMPOSITES

1. INTRODUCTION

A large number of reinforced concrete bridges in the U.S. are structurally deficient or obsolete. The main contributing factors are changes in their use, an increase in load requirements or corrosion deterioration due to exposure to an aggressive environment. In order to preserve those bridges, rehabilitation is often considered essential to maintain their capability and to increase public safety (Seible et al., 1995; Kachlakev, 1998).

In the last decade, fiber reinforced polymer (FRP) composites have been used for strengthening structural members of reinforced concrete bridges. Many researchers have found that FRP composites applied to those members provide efficiency, reliability and cost effectiveness in rehabilitation (Marshall and Busel, 1996; Steiner 1996; Tedesco et al., 1996; Kachlakev, 1998). Currently in the U.S., ACI Committee 440 is working to establish design recommendations for FRP application to reinforced concrete (ACI 440, 2000).

Since in many cases the currently available design and simplified analysis tools cannot provide complete and accurate predictions, the Finite Element Method (FEM) is employed in this study of the behavior of reinforced concrete members strengthened with FRP composites. In this research, the ANSYS finite element program (ANSYS 5.5: ANSYS, Inc., 1998) is used to simulate the behavior of four full-scale reinforced concrete beams tested at Oregon State University (Kachlakev and McCurry, 2000).

1.1. Transverse Beams of Horsetail Creek Bridge

Four full-scale reinforced concrete beams were fabricated at Oregon State University. The beams replicated transverse members from the Horsetail Creek Bridge, constructed in 1913. The bridge is in current use, located east of Portland, Oregon along the Historic Columbia River Highway, and is a historic structure. Load rating of the bridge revealed that the transverse beams were constructed without the presence of shear reinforcement (Kachlakev and McCurry, 2000). Moreover, the load rating showed that the beams were deficient both in shear and flexural capacity (CH2M HILL, 1997). The Oregon Department of Transportation (ODOT) resolved to utilize FRP composites to reinforce the beams. Strengthening the beams with FRP composites was considered advantageous due to the historic nature of the bridge, limited funding and time restrictions. Two types of FRP composites, i.e. Glass Fiber Reinforced Polymer (GFRP) and Carbon Fiber Reinforced Polymer (CFRP), have been used to reinforce the beams. GFRP and CFRP composites were applied in different thicknesses and at various locations depending upon the capacity needed for the beams. GFRP was applied on the sides of the beams to provide increased shear strength, whereas CFRP was added to the bottom of the beams for additional flexural strength.

1.2. Background

Typically, the behavior of reinforced concrete beams is studied by experimental investigations on full-scale beams. The results are compared to theoretical calculations, which estimate deflections and internal stress/strain distributions within the beams.

Finite element analysis can also be used to model the behavior numerically and help to confirm these calculations, as well as to provide a valuable supplement to the laboratory investigations of behavior, particularly in parametric studies.

Modeling the complex behavior of reinforced concrete, which is both nonhomogeneous and anisotropic, is one of the most difficult challenges in the finite element analysis of civil engineering structures. Most early finite element models of reinforced concrete included the effects of cracking based on a pre-defined crack pattern (Ngo and Scordelis, 1967; Nilson, 1968). With this approach, changes in the topology of the models were required as the load increased; therefore, the ease and speed of the analysis were limited.

A smeared cracking approach was introduced using isoparametric formulations to represent the cracked concrete as an orthotropic material (Rashid, 1968). In the smeared cracking approach, cracking of the concrete occurs when the principal tensile stress exceeds the ultimate tensile strength. The elastic modulus of the material is then assumed to be zero in the direction parallel to the principal tensile stress direction (Suidan and Schnobrich, 1973).

Only recently have researchers attempted to simulate the behavior of reinforced concrete strengthened with FRP composites using the finite element method. A number of reinforced concrete beams strengthened with FRP plates were tested in the laboratory. Finite element analysis with the smeared cracking approach was used to simulate the behavior and failure mechanisms of those experimental beams (Arduini et al., 1997). Comparisons between the experimental data and the results from finite element models showed good agreement, and the different failure mechanisms, from

ductile to brittle, could be simulated. However, the FRP plates were modeled with two-dimensional plate elements in this study, and the crack patterns of those beams were not predicted by the finite element analysis. The two-dimensional plate elements are surface-like elements, which have no actual thicknesses. Therefore, stress and strain results at the actual surfaces of the FRP plates were estimated by theoretical calculations.

In addition, an entire FRP strengthened reinforced concrete bridge was modeled by finite element analysis (Tedesco et al., 1999). In this study, truss elements were used to model the FRP composites. The results of the finite element analysis correlated well with the field test data and indicated that the external bonding of FRP laminates to the bridge girders reduced the average maximum deflections at midspan and reinforcing steel stresses by 9% and 11%, respectively.

The current study presents results from the finite element analysis of the four full-scale Horsetail Creek Bridge reinforced concrete beams. The finite element model uses a smeared cracking approach and three-dimensional layered elements to model FRP composites. Comparisons between finite element results and those from the experimental beams are shown. Crack patterns obtained from the finite element analysis are compared to those observed for the experimental beams.

1.3. Objectives

The objective of this study is to simulate and analyze the behavior of four full-scale reinforced concrete beams by using the ANSYS finite element analysis program (ANSYS 5.5: ANSYS, Inc., 1998) both before and after the application of FRP

composites. The beams replicate the transverse beams of the Horsetail Creek Bridge tested at Oregon State University (Kachlakev and McCurry, 2000).

1.4. Scope

Four full-scale reinforced concrete beams (similar to the transverse beams of the Horsetail Creek Bridge) were fabricated and tested at Oregon State University (Kachlakev and McCurry, 2000). The four beams were constructed with different FRP reinforcing schemes to compare the effects of each on behavior in the laboratory. The beams were as follows: control, flexural strengthened, shear strengthened, and flexural/shear strengthened beams. The control beam was a reinforced concrete beam with no shear stirrups and no FRP reinforcement. The flexural strengthened beam was a control beam with added CFRP reinforcing on the bottom of the beam. The shear strengthened beam was a control beam with added GFRP reinforcing on the sides of the beam. The flexural/shear strengthened beam was a control beam with added CFRP reinforcing on the bottom and GFRP reinforcing on the sides of the beam. Finite element models were developed to simulate the behaviors of each of the four experimental beams from linear through nonlinear response and up to failure using the ANSYS program (ANSYS 5.5: ANSYS, Inc., 1998). Results obtained from the finite element models are presented and compared with the experimental data. Comparisons are made for load-strain plots at selected locations on the beams; load-deflection plots at midspan, first cracking loads; loads at failure; and crack patterns at failure. Conclusions and recommendations for future research are also presented.

2. FINITE ELEMENT MODELING

The ANSYS finite element program (ANSYS 5.5: ANSYS, Inc., 1998) operating on a UNIX system was used in this study to simulate the behavior of the four experimental beams.

2.1. Element Types

2.1.1. Reinforced Concrete

An eight-node solid element, Solid65, is used to model the concrete. The solid element has eight nodes with three degrees of freedom at each node, translations in the nodal x, y, and z directions. The element is capable of plastic deformation, cracking in three orthogonal directions, and crushing. The geometry and node locations for this element type are shown in Figure 2.1.

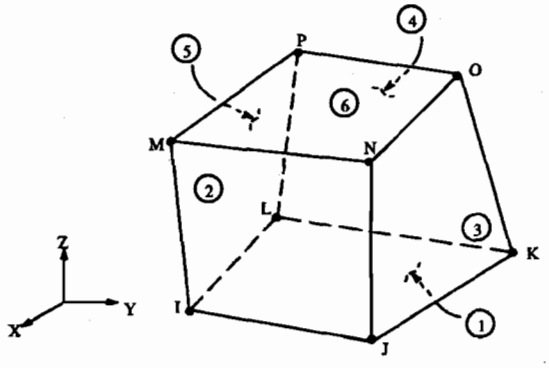

Figure 2.1: Solid65 3-D Reinforced Concrete Solid (ANSYS, 1998)

A Link8 element is used to model the steel reinforcement. Two nodes are required for this element. Each node has three degrees of freedom, i.e., translations in the nodal x, y, and z directions. The element is also capable of plastic deformation. The geometry and node locations for this element type are shown in Figure 2.2.

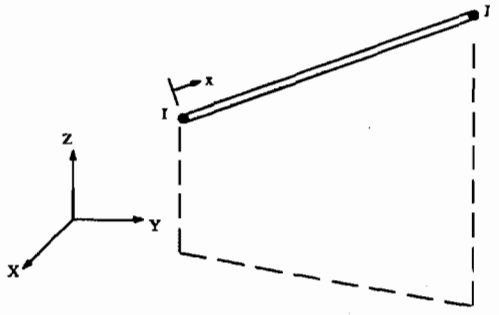

Figure 2.2: Link8 3-D Spar (ANSYS, 1998)

2.1.2. FRP Composites

A layered solid element, Solid46, is used to model the FRP composites. The element allows for up to 100 different material layers with different orientations, and orthotropic material properties in each layer. The element has three degrees of freedom at each node, translations in the nodal x, y, and z directions. The geometry, node locations, and the coordinate system are shown in Figure 2.3.

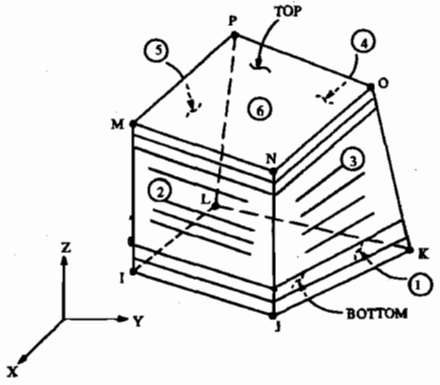

Figure 2.3: Solid46 3-D Layered Structural Solid (ANSYS, 1998)

2.1.3. Steel Plates

An eight-node solid element, Solid45, is used for the steel plates in the model. The element is defined with eight nodes having three degrees of freedom at each node, translations in the nodal x, y, and z directions. The geometry and node locations for this element type are shown in Figure 2.4.

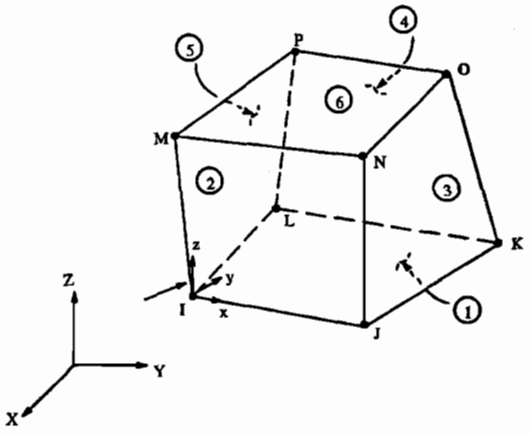

Figure 2.4: Solid45 3-D Solid (ANSYS, 1998)

2.2. Material Properties

2.2.1. Concrete

Development of a model for the behavior of concrete is a challenging task. Concrete is a quasi-brittle material and has different behavior in compression and tension. The tensile strength of concrete is typically 8-15% of the compressive strength (Shah et al., 1995). Figure 2.5 shows a typical stress-strain curve for normal weight concrete (Bangash, 1989).

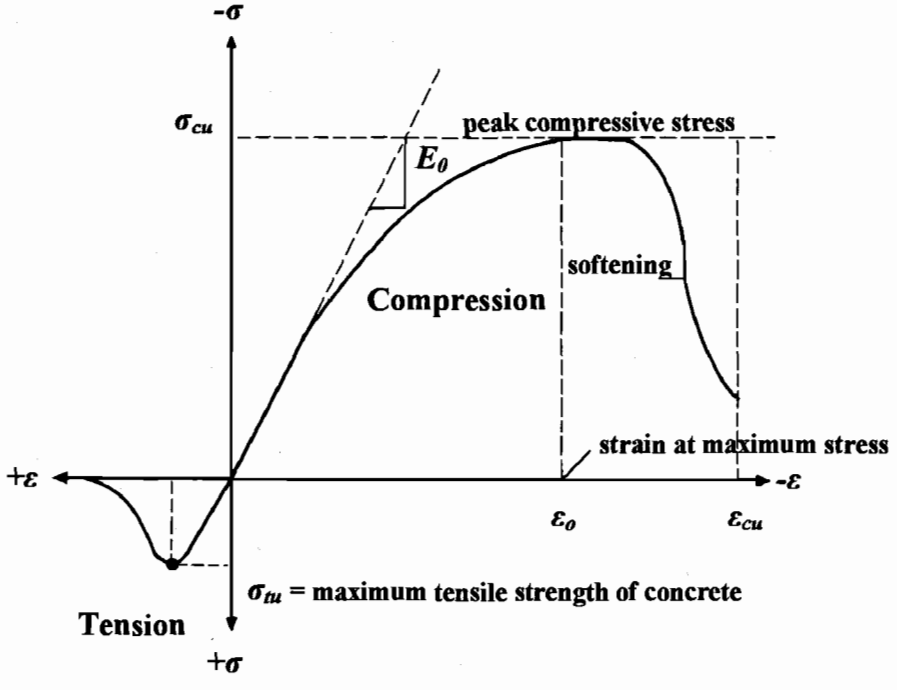

Figure 2.5: Typical Uniaxial Compressive and Tensile Stress-Strain Curve for Concrete (Bangash, 1989)

In compression, the stress-strain curve for concrete is linearly elastic up to about 30 percent of the maximum compressive strength. Above this point, the stress increases gradually up to the maximum compressive strength. After it reaches the maximum compressive strength σ_{cu}, the curve descends into a softening region, and eventually crushing failure occurs at an ultimate strain ε_{cu}. In tension, the stress-strain curve for concrete is approximately linearly elastic up to the maximum tensile strength. After this point, the concrete cracks and the strength decreases gradually to zero (Bangash, 1989).

2.2.1.1. FEM Input Data

A concrete material model, available in ANSYS, is used in this study. The program requires input data for concrete material properties as follows:

- Elastic modulus (E_c).
- Ultimate uniaxial compressive strength (f'_c).
- Ultimate uniaxial tensile strength (Modulus of rupture, f_r).
- Poisson's ratio (ν).
- Shear transfer coefficient (β_t).
- Compressive uniaxial stress-strain relationship for concrete.

For the full-scale beam tests (Kachlakev and McCurry, 2000), an effort was made to accurately estimate the actual elastic modulus of the beams using the ultrasonic pulse velocity method (ASTM 1983,1994). A correlation was made between pulse velocity and compressive elastic modulus following the ASTM standard methods.

From this work, it was noted that each experimental beam had a slightly different elastic modulus; therefore, these values are used in the finite element modeling.

From the elastic modulus obtained by the pulse velocity method, the ultimate concrete compressive and tensile strengths for each beam model were calculated by Equations 2-1, and 2-2, respectively (ACI 318, 1999).

$$f_c' = \left(\frac{E_c}{57000}\right)^2 \qquad \textbf{(2-1)}$$

$$f_r = 7.5\sqrt{f_c'} \qquad \textbf{(2-2)}$$

where:

E_c = elastic modulus of concrete, psi
f_c' = ultimate compressive strength, psi
f_r = ultimate tensile strength (modulus of rupture), psi

Poisson's ratio for concrete is assumed to be 0.2 (Bangash, 1989) and is used for all four beams. The shear transfer coefficient, β_t represents conditions of the crack face. The value of β_t ranges from 0.0 to 1.0, with 0.0 representing a smooth crack (complete loss of shear transfer) and 1.0 representing a rough crack (no loss of shear transfer) (ANSYS, 1998). However, the value of β_t used in many studies of reinforced concrete structures varied between 0.05 and 0.25 (Bangash, 1989; Huyse et al., 1994; Hemmaty, 1998). The shear transfer coefficient used in this study is equal to 0.2. A summary of the concrete properties used in this finite element modeling study is shown in Table 2.1.

Table 2.1: Summary of Material Properties for Concrete

Beam	E_c (ksi)*	f_c' (psi)	f_r (psi)	ν	β_t
Control beam	2,806	2,423	369.2	0.2	0.2
Flexural beam	2,545	1,994	334.9	0.2	0.2
Shear beam	2,634	2,136	346.6	0.2	0.2
Flexural/Shear beam	2,477	1,889	325.9	0.2	0.2

*From pulse velocity measurements (Kachlakev and McCurry, 2000)

2.2.1.2. Compressive Uniaxial Stress-Strain Relationship for Concrete

The ANSYS program requires the uniaxial stress-strain relationship for concrete in compression. Numerical expressions (Desayi and Krishnan, 1964), Equations 2-3 and 2-4, are used along with Equation 2-5 (Gere and Timoshenko, 1997) to construct the uniaxial compressive stress-strain curve for concrete in this study.

$$f = \frac{E_c \varepsilon}{1 + \left(\frac{\varepsilon}{\varepsilon_0}\right)^2} \qquad \textbf{(2-3)}$$

$$\varepsilon_0 = \frac{2 f'_c}{E_c} \qquad \textbf{(2-4)}$$

$$E_c = \frac{f}{\varepsilon} \qquad \textbf{(2-5)}$$

where:

f = stress at any strain ε, psi
ε = strain at stress f
E_c = concrete elastic modulus, psi
ε_0 = strain at the ultimate compressive strength f_c'

Figure 2.6 shows the simplified compressive uniaxial stress-strain relationship that is used in this study.

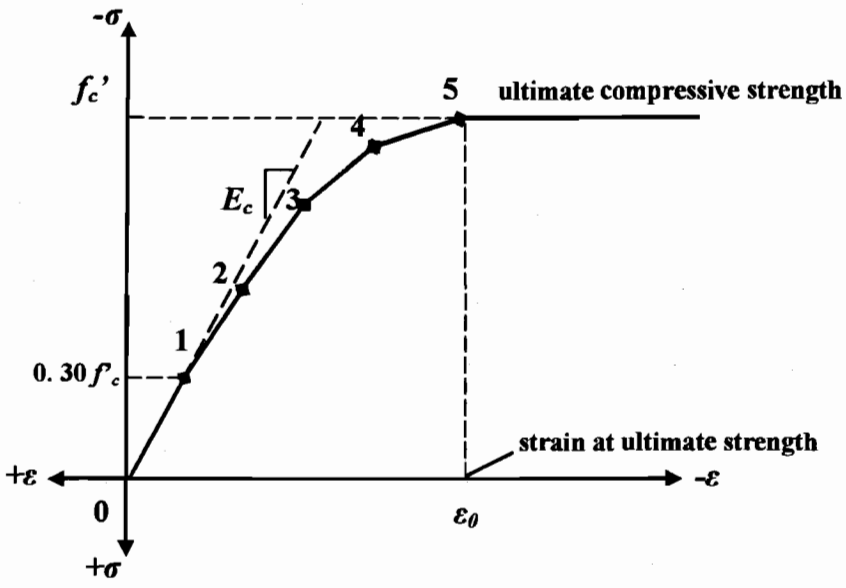

Figure 2.6: Simplified Compressive Uniaxial Stress-Strain Curve for Concrete

The simplified stress-strain curve for each beam model is constructed from six points connected by straight lines. The curve starts at zero stress and strain. Point No.1, at 0.30 f'_c, is calculated for the stress-strain relationship of the concrete in the linear range (Equation 2-5). Points 2, 3, and 4 are obtained from Equation 2-3, in which ε_0 is calculated from Equation 2-4. Point No. 5 is at ε_0 and f'_c. In this study, an assumption of perfectly plastic behavior is made after point No.5.

An example is included here to demonstrate a calculation of the five points (1-5) on the curve using the control beam model. The model has a concrete elastic modulus of 2,806,000 psi. f'_c calculated by Equation 2-1 is equal to 2423 psi. For point No.1,

strain at a stress of 727 psi ($0.3\,f'_c$) is obtained for a linear stress-strain relationship for concrete (Equation 2-5), and is 0.00026 in./in. Strain at the ultimate compressive strength, ε_0 is calculated by Equation 2-4, and equals 0.00173 in./in. Points 2, 3, and 4 are calculated from Equation 2-3, which gives strains of 0.00060, 0.00095 and 0.00130 in./in., corresponding to stresses of 1502, 2046 and 2328 psi, respectively. Finally, point No.5 is at the ultimate strength, f'_c of 2423 psi and ε_0 of 0.00173 in./in.

2.2.1.3. Failure Criteria for Concrete

The model is capable of predicting failure for concrete materials. Both cracking and crushing failure modes are accounted for. The two input strength parameters, i.e. ultimate uniaxial tensile and compressive strengths, are needed to define a failure surface for the concrete. Consequently, a criterion for failure of the concrete due to a multiaxial stress state can be calculated (William and Warnke, 1975). Note that the concrete will crack if the principal tensile stress lies outside the failure surface, while crushing will occur only if all principal stresses are compressive and lie outside the failure surface.

A three-dimensional failure surface for concrete is shown in Figure 2.7. The most significant nonzero principal stresses are in the x and y directions, represented by σ_{xp} and σ_{yp}, respectively. Three failure surfaces are shown as projections on the σ_{xp}-σ_{yp} plane. The mode of failure is a function of the sign of σ_{zp} (principal stress in the z direction). For example, if σ_{xp} and σ_{yp} are both negative (compressive) and σ_{zp} is slightly positive (tensile), cracking would be predicted in a direction perpendicular to

σ_{zp}. However, if σ_{zp} is zero or slightly negative, the material is assumed to crush (ANSYS, 1998).

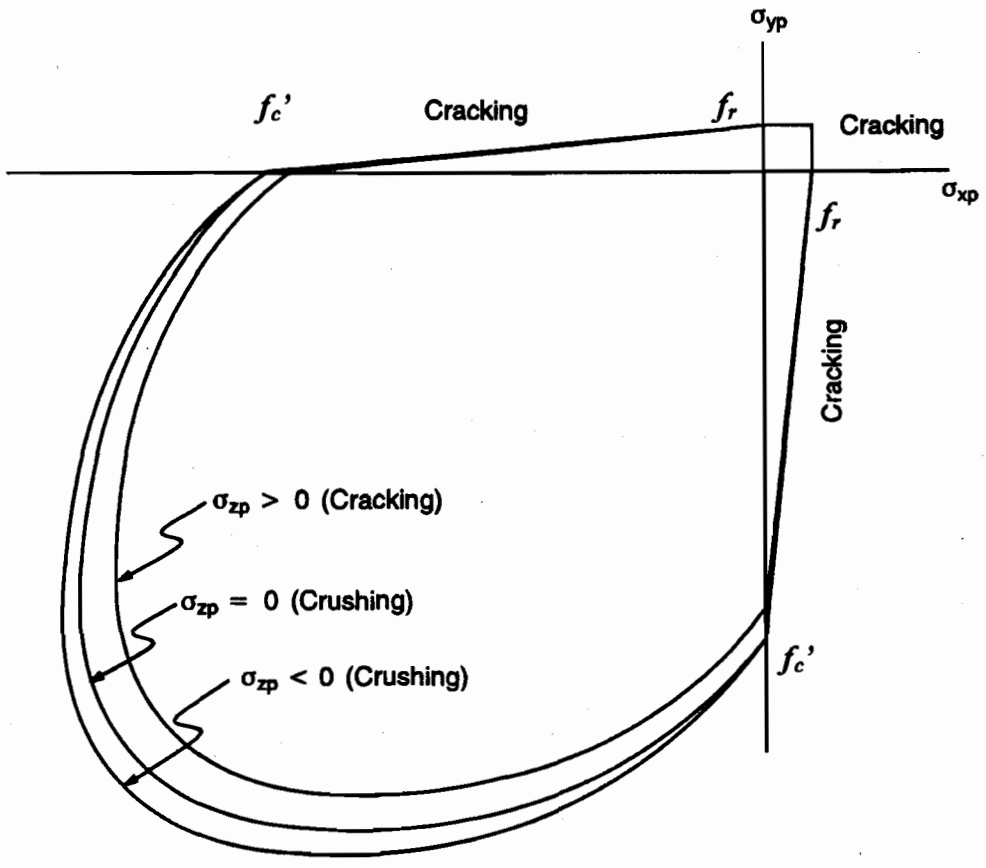

Figure 2.7: 3-D Failure Surface for Concrete (ANSYS, 1998)

In a concrete element, cracking occurs when the principal tensile stress in any direction lies outside the failure surface. After cracking, the elastic modulus of the concrete element is set to zero in the direction parallel to the principal tensile stress direction. Crushing occurs when all principal stresses are compressive and lie outside

the failure surface, subsequently, the elastic modulus is set to zero in all directions (ANSYS, 1998), and the element effectively disappears.

During this study, it was found that if the crushing capability of the concrete is turned on, the finite element models fail prematurely. Crushing of the concrete started to develop in elements located under the loads. Subsequently, adjacent concrete elements crushed rapidly within several load steps. Soon after, the model showed a large displacement, and the solution for the model diverged. A pure "compression" failure of concrete is somewhat suspicious. In a compression test, the specimen is subjected to a uniaxial compressive load. Secondary tensile strains induced by Poisson's effect occur perpendicular to the load. Since concrete is relatively weak in tension, these cause cracking and the failure (Mindess and Young, 1981; Shah et al., 1995). Therefore, in this study, the crushing capability was turned off and cracking of the concrete controls the failure of the finite element models.

2.2.2. Steel Reinforcement and Steel Plates

Steel reinforcement in the experimental beams was constructed with typical Grade 60 steel reinforcing bars. Properties, i.e. elastic modulus and yield stress, for the steel reinforcement used in this FEM study follow the design material properties used for the experimental investigation (Kachlakev and McCurry, 2000). The steel for the finite element models is assumed to be an elastic-perfectly plastic material and identical in tension and compression. Poisson's ratio of 0.3 is used for the steel reinforcement in this study (Gere and Timoshenko, 1997). Figure 2.8 shows the stress-strain relationship

used in this study. Material properties for the steel reinforcement for all four models are as follows:

- Elastic modulus, E_s = 29,000 ksi
- Yield stress, f_y = 60,000 psi
- Poisson's ratio, ν = 0.3

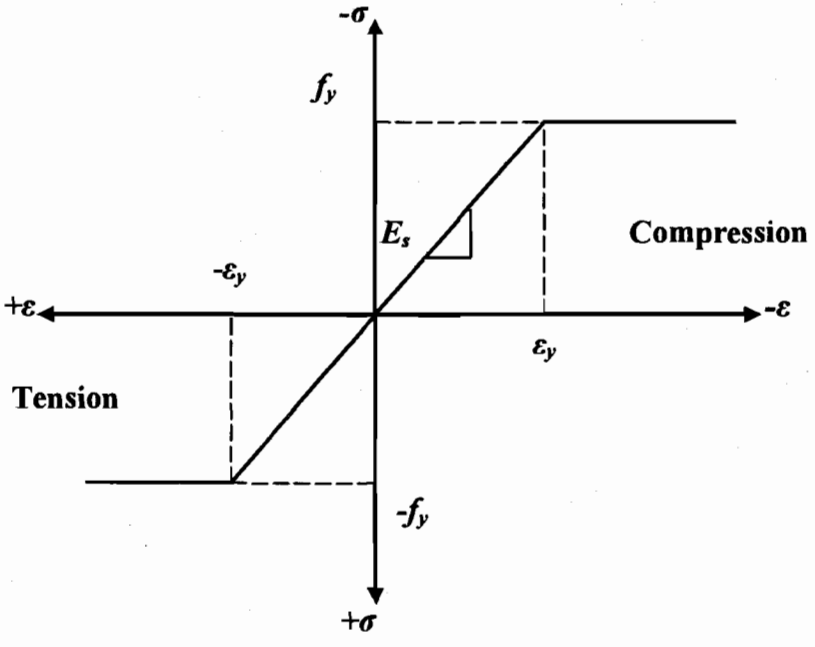

Figure 2.8: Stress-Strain Curve for Steel Reinforcement

Steel plates are added at support locations in the finite element models to provide a more even stress distribution over the support areas. An elastic modulus equal to 29,000 ksi and Poisson's ratio of 0.3 are used for the plates (Gere and Timoshenko, 1997). The steel plates are assumed to be linear elastic materials.

2.2.3. FRP Composites

FRP composites are materials that consist of two constituents. The constituents are combined at a macroscopic level and are not soluble in each other. One constituent is called the reinforcing phase and the one in which it is embedded is called the matrix (Kaw, 1997). The reinforcing phase material is in the form of fibers, i.e. carbon and glass, which are typically stiffer and stronger. The matrix phase material or polymer is generally continuous, less stiff and weaker. The FRP composites are anisotropic materials, that is, their properties are not the same in all directions. Figure 2.9 shows a schematic of the FRP composites.

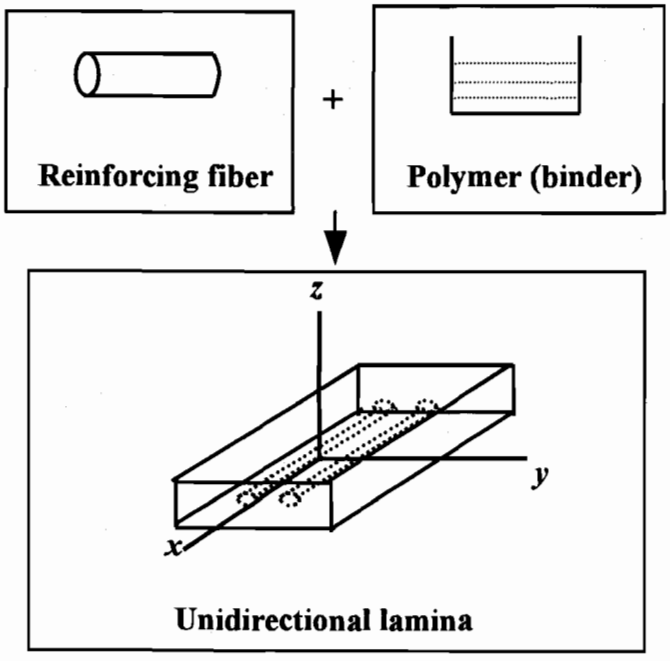

Figure 2.9: Schematic of FRP Composites (Gibson, 1994; Kaw, 1997)

As shown in Figure 2.9, the unidirectional lamina has three mutually orthogonal planes of material properties (i.e., *xy*, *xz*, and *yz* planes). The *xyz* coordinate axes are referred to as the principal material coordinates where the *x* direction is the same as the fiber direction, and the *y* and *z* directions are perpendicular to the *x* direction. It is a so-called specially orthotropic material (Gibson, 1994; Kaw, 1997). In this study, the specially orthotropic material is also transversely isotropic, where the properties of the FRP composites are nearly the same in any direction perpendicular to the fibers, thus the properties in the *y* direction are the same as those in the *z* direction.

Two types of FRP composites have been used to reinforce the four full-scale beams (McCurry and Kachlakev, 2000). Glass Fiber Reinforced Polymer (GFRP) is applied on the sides of the beams for increased shear strength, due to its superior strain at failure. Carbon Fiber Reinforced Polymer (CFRP) is employed on the bottom of the beams to provide added flexural strength, due to its high tensile strength. Linear elastic properties of FRP composites are assumed throughout this study. Figure 2.10 shows stress-strain curves for the FRP composites used in this study.

Input data needed for the FRP composites in the finite element models are as follows:

- Number of layers.
- Thickness of each layer.
- Orientation of the fiber direction for each layer.
- Elastic modulus of the FRP composite in three directions (E_x, E_y, and E_z).
- Shear modulus of the FRP composite for three planes (G_{xy}, G_{yz}, and G_{xz}).
- Major Poisson's ratio for three planes (ν_{xy}, ν_{yz}, and ν_{xz}).

Note that a local coordinate system for the FRP layered solid elements is defined where the x direction is the same as the fiber direction, while the y and z directions are perpendicular to the x direction.

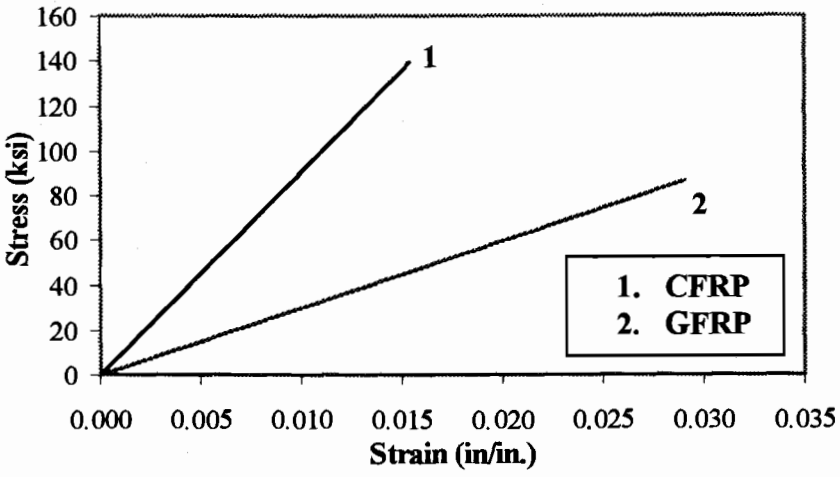

Figure 2.10: Stress-Strain Curves for Unidirectional FRP Composites Under Uniaxial Tensile Load Along Fibers (Kachlakev and McCurry, 2000)

The properties of isotropic materials, such as elastic modulus and Poisson's ratio, are identical in all directions, therefore no subscripts are required. This is not the case with specially orthotropic materials. Subscripts are needed to define properties in the various directions. For example, $E_x \neq E_y$ and $\nu_{xy} \neq \nu_{yx}$. E_x is the elastic modulus in the fiber direction, and E_y is the elastic modulus in the y direction perpendicular to the fiber direction. The use of Poisson's ratios for orthotropic materials often causes confusion; therefore the orthotropic material data are supplied in the ν_{xy} or major Poisson's ratio format for the ANSYS program. The major Poisson's ratio is the ratio of strain in the y direction to strain in the perpendicular x direction when the applied

stress is in the x direction. ν_{yx} is called a minor Poisson's ratio, and is smaller than ν_{xy}, where E_x is larger than E_y. Equation 2-6 shows the relationship between ν_{xy} and ν_{yx} (Kaw, 1997).

$$\nu_{yx} = \frac{E_y}{E_x}\nu_{xy} \tag{2-6}$$

where:

ν_{yx} = Minor Poisson's ratio
E_x = Elastic modulus in the x direction (fiber direction)
E_y = Elastic modulus in the y direction
ν_{xy} = Major Poisson's ratio

A summary of material properties used for the modeling of all four beams is shown in Table 2.2.

Table 2.2: Summary of Material Properties for FRP Composites (Kachlakev and McCurry, 2000)

FRP composite	Elastic modulus (ksi)	Major Poisson's ratio	Tensile strength (ksi)	Shear modulus (ksi)	Thickness of laminate (in.)
CFRP	$E_x = 9000$ $E_y = 700.0$* $E_z = 700.0$*	$\nu_{xy} = 0.22$ $\nu_{xz} = 0.22$ $\nu_{yz} = 0.30$*	139.0	$G_{xy} = 474.0$* $G_{xz} = 474.0$* $G_{yz} = 270.0$**	0.04
GFRP	$E_x = 3000$ $E_y = 1000$* $E_z = 1000$*	$\nu_{xy} = 0.26$ $\nu_{xz} = 0.26$ $\nu_{yz} = 0.30$*	87.00	$G_{xy} = 220.0$ $G_{xz} = 220.0$ $G_{yz} = 385.0$**	0.05

*(Kachlakev, 1998)

** $G_{yz} = \dfrac{E_{y\ or\ z}}{2(1+\nu_{yz})}$

2.3. Modeling Methodology

Finite element models of the four experimental beams, derived from the transverse beams of the Horsetail Creek Bridge, were developed to investigate their behavior under loading using the ANSYS program. The four experimental beams were constructed and tested at Oregon State University. One beam was a control, whereas the other three beams were constructed with different FRP reinforcing schemes (McCurry and Kachlakev, 2000; Kachlakev and McCurry, 2000).

2.3.1. Geometry

A solid element, Solid65, is used for the concrete in the finite element models. The dimensions of the experimental beams are $12in. \times 240in. \times 30.25in.$ The span between the two supports is 216 in. Figure 2.11 illustrates typical dimensions for all four beams before FRP reinforcing. By taking advantage of the symmetry of the beams, a quarter of the full beam is used for modeling. This approach reduces computational time and computer disk space requirements significantly. The quarter of the entire model is shown in Figure 2.12.

Figure 2.13 shows typical steel reinforcement locations for the experimental beams. In the finite element models, 3-D spar elements, Link8, are employed to represent the steel reinforcement, referred to here as link elements. The steel reinforcement is simplified in the model by ignoring the inclined portions of the steel bars present in the test beams. Figure 2.14 shows typical steel reinforcement for a quarter beam model.

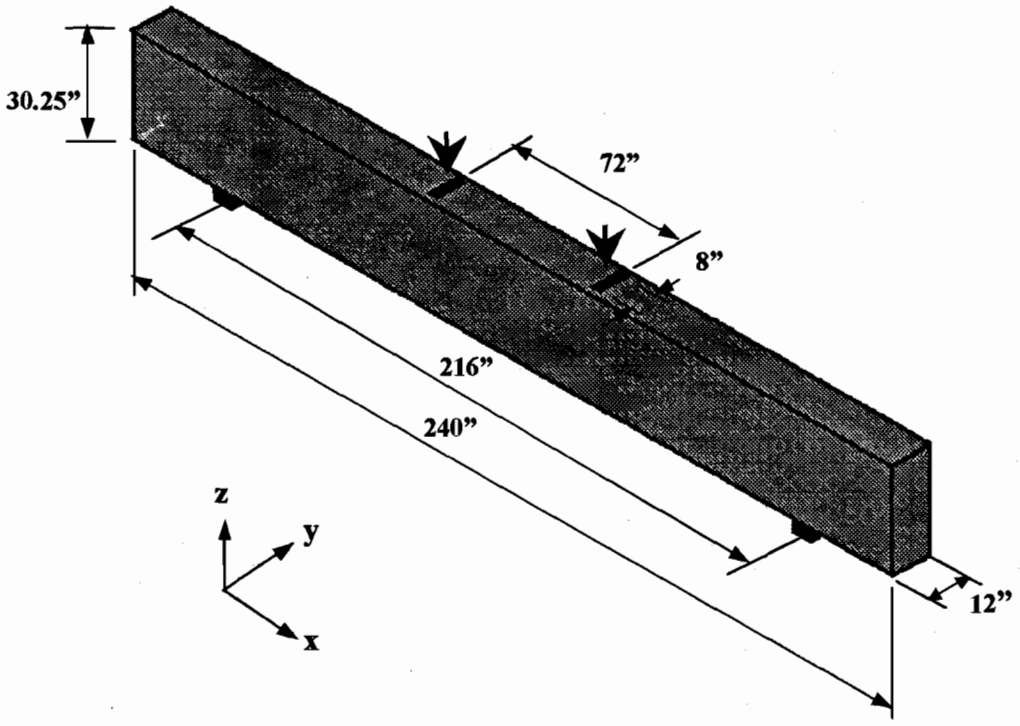

Figure 2.11: Typical Beam Dimensions (not to scale)

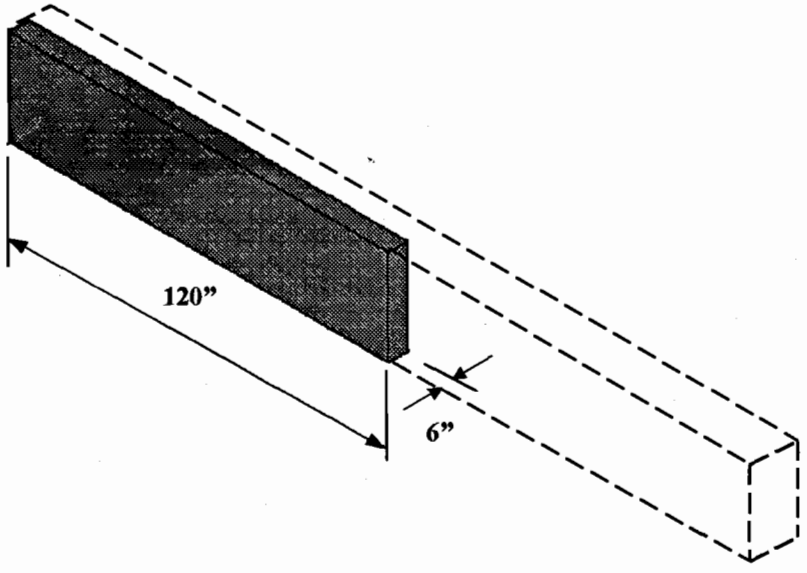

Figure 2.12: Use of a Quarter Beam Model (not to scale)

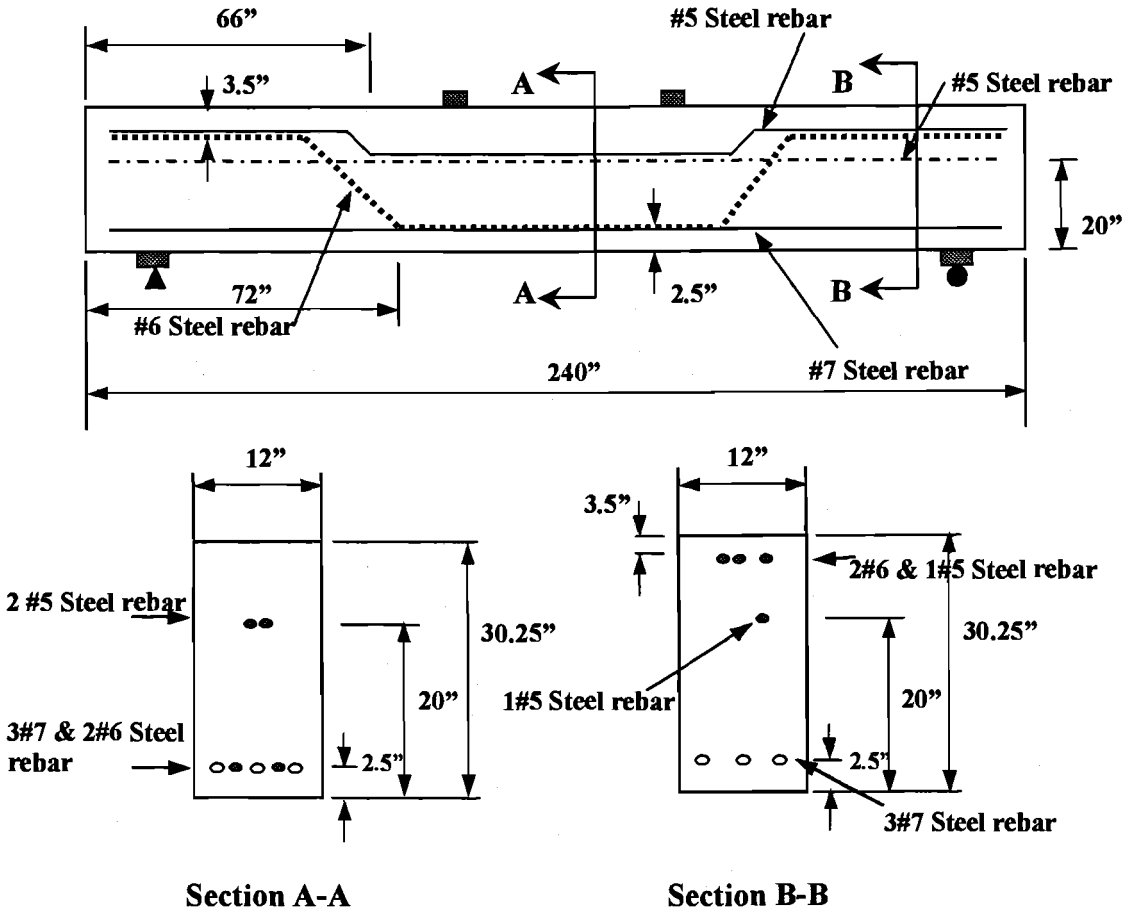

Figure 2.13: Typical Steel Reinforcement Locations (not to scale)
(McCurry and Kachlakev, 2000)

Ideally, the bond strength between the concrete and steel reinforcement should be considered. However, in this study, perfect bond between materials is assumed. To provide the perfect bond, the link element for the steel reinforcing is connected between nodes of each adjacent concrete solid element, so the two materials share the same nodes. The same approach is adopted for FRP composites. Since the epoxy used to attach FRP sheets to the experimental beams has a sufficiently high strength, this supports the perfect bond assumption.

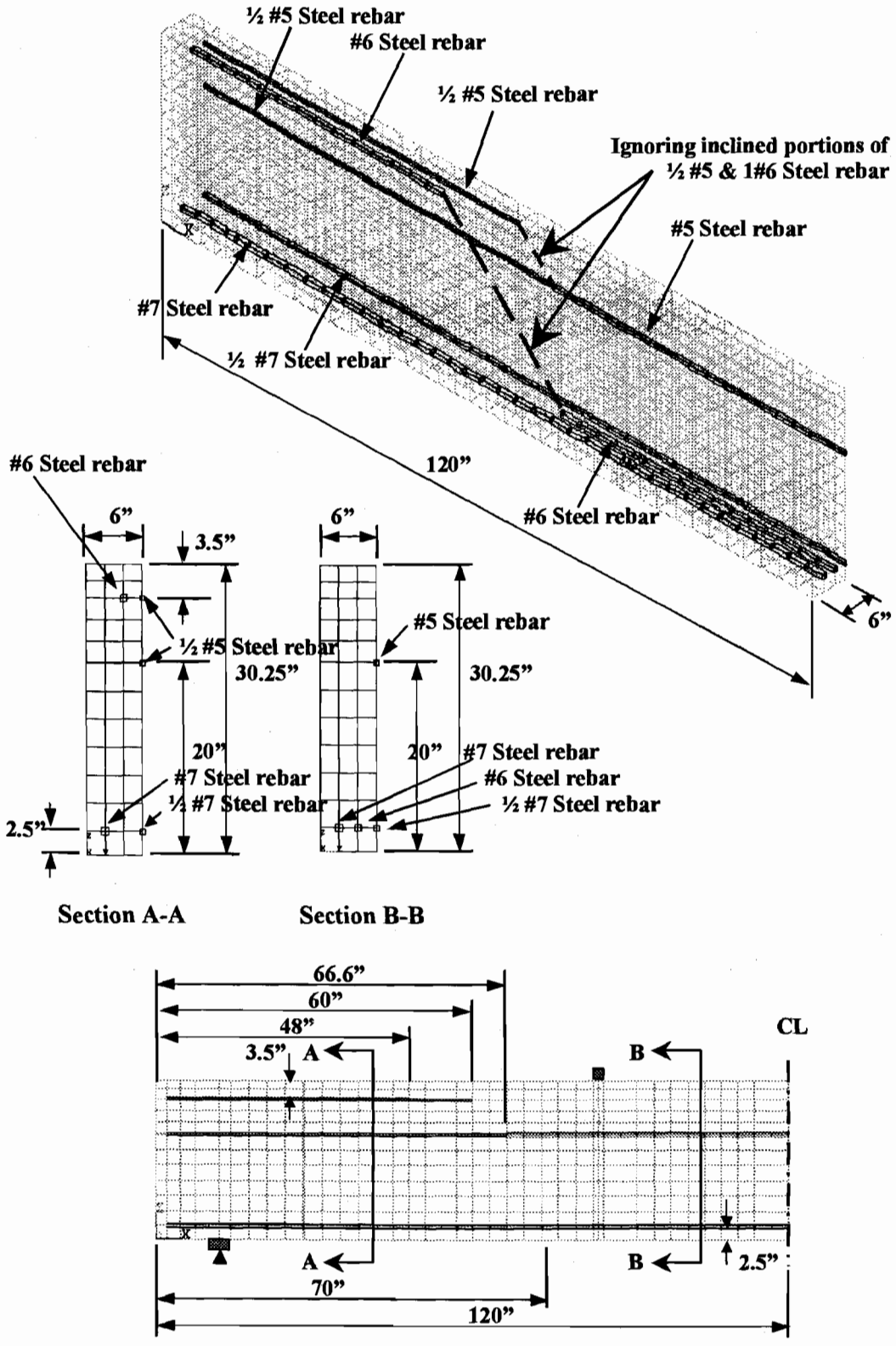

Figure 2.14: Typical Steel Reinforcement for a Quarter Beam Model (not to scale)

In the finite element models, layered solid elements, Solid46, are used to model the FRP composites. Nodes of the FRP layered solid elements are connected to those of adjacent concrete solid elements in order to satisfy the perfect bond assumption. Figure 2.15 illustrates the element connectivity.

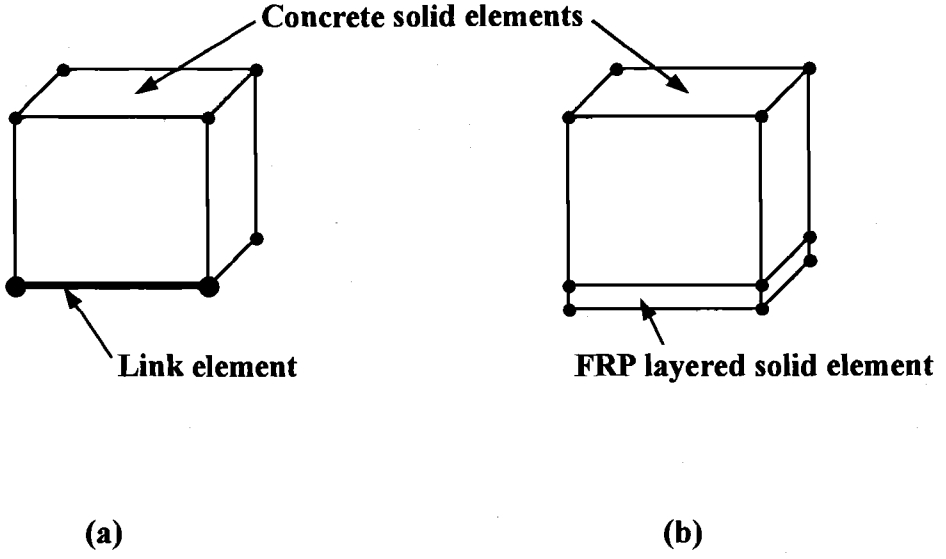

Figure 2.15: Element Connectivity: (a) Concrete Solid and Link Elements; (b) Concrete Solid and FRP Layered Solid Elements

Reinforcing schemes for the experimental strengthened beams are shown in Figure 2.16. GFRP and CFRP composite laminates have various thicknesses depending upon the capacities needed at various locations on the beams.

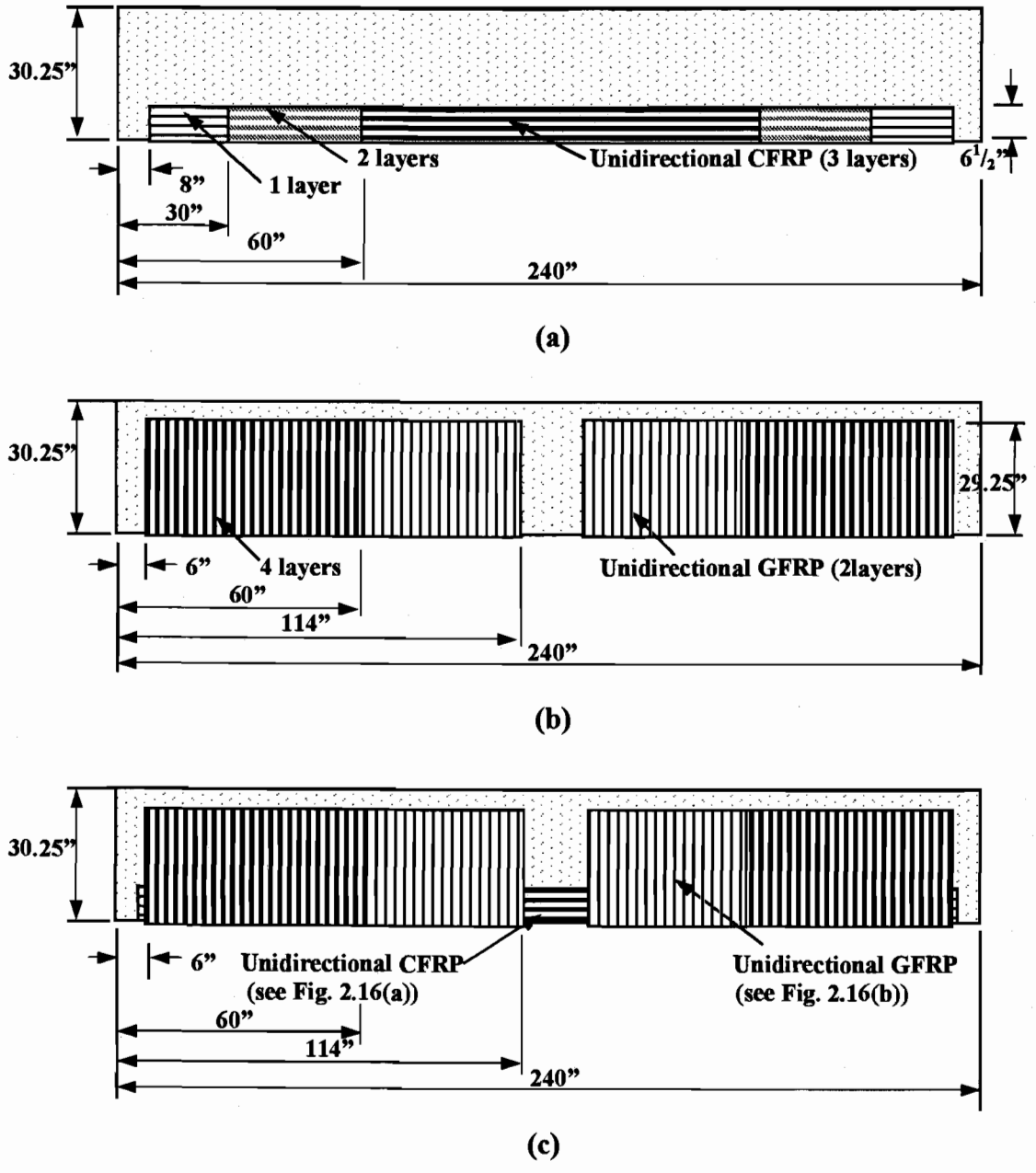

Figure 2.16: FRP Reinforcing Schemes (not to scale)**: (a) Flexural Strengthened Beam; (b) Shear Strengthened Beam; (c) Flexural/Shear Strengthened Beam** (McCurry and Kachlakev, 2000)

The various thicknesses of the FRP composites create discontinuities, which are not desirable for the finite element analysis. These may develop high stress

concentrations at local areas on the models; consequently, when the model is run, the solution may have difficulties in convergence. Therefore, a consistent thickness of FRP composites is used in the models to avoid discontinuities, by compensating with changes in the elastic and shear moduli in each layer. For example, if the thickness of FRP laminates is doubled, the elastic and shear moduli are reduced by 50%. Note that the relationship between elastic and shear moduli is linear. Equation 2-7 shows the relationship between elastic and shear moduli (ANSYS, 1998).

$$G_{xy} = \frac{E_x E_y}{E_x + E_y + 2\nu_{xy} E_x} \tag{2-7}$$

where:

G_{xy} = Shear modulus in the xy plane
E_x = Elastic modulus in the x direction
E_y = Elastic modulus in the y direction
ν_{xy} = Major Poisson's ratio

For this study, minor modification of dimensions for the FRP reinforcing was made due to geometric constraints from the other elements in the models, i.e. meshing of concrete elements, steel rebar locations and required output locations. Figure 2.17 shows the modified dimensions of the FRP reinforcing schemes for the quarter beam models.

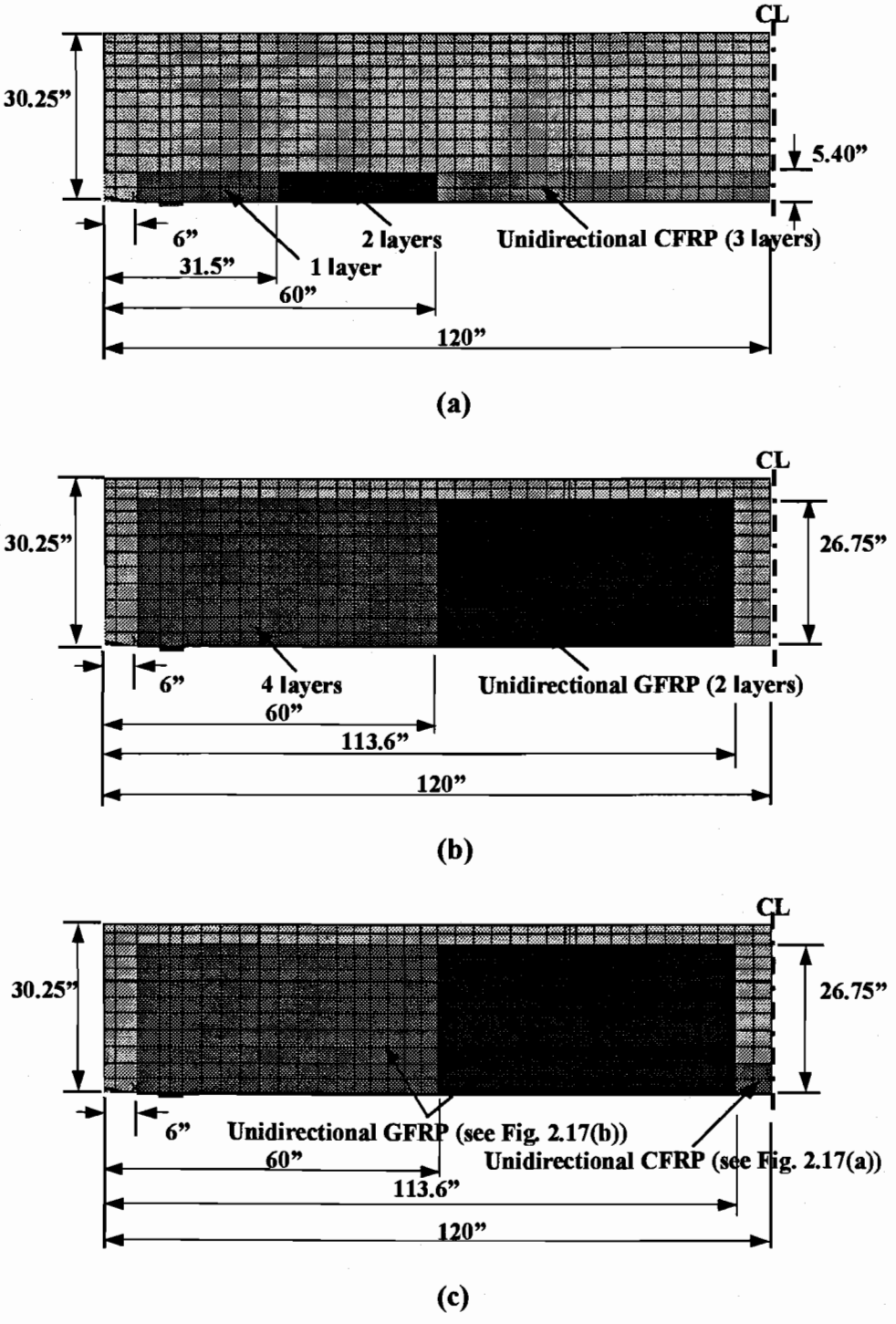

Figure 2.17: Modified Dimensions of FRP Reinforcing for Strengthened Beam Models (not to scale): **(a) Flexural Strengthened Beam; (b) Shear Strengthened Beam; (c) Flexural/Shear Strengthened Beam**

2.3.2. Meshing

As an initial step, a finite element analysis requires meshing on the model. In other words, the model is divided into a number of small elements, and after loading, stress and strain are calculated at integration points of these small elements (Bathe, 1996). An important step in finite element modeling is the selection of the mesh density. A convergence of results is obtained with an adequate number of elements in a model. This is practically achieved if when the mesh density increases, a negligible effect on the results occurs (Adams and Askenazi, 1998). Therefore, in this finite element modeling study, a convergence study was carried out to determine an appropriate mesh density.

The convergence study employed a control beam model with four different numbers of elements, i.e. 896, 1136, 1580 and 2264, to examine the convergence of the results. Three parameters at different locations were used to see if the results converged. The outputs were collected at the same applied load, and are as follows: deflection at midspan; compressive stress in concrete at midspan at the center of the top face of the beam models; and tensile stress in the main steel reinforcement at midspan. Figure 2.18 shows the results from the convergence study.

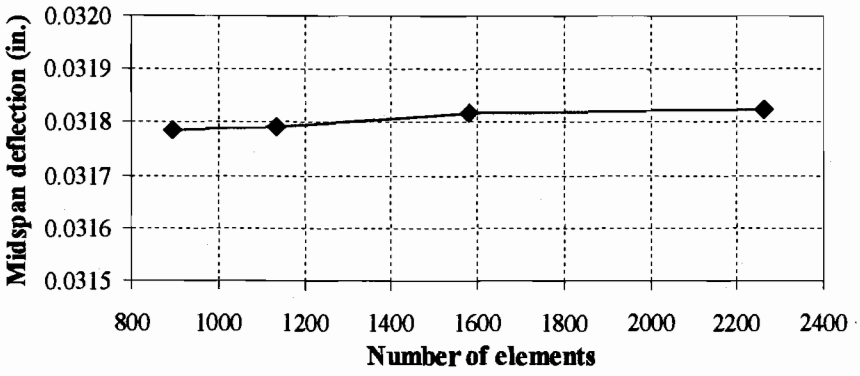

(a)

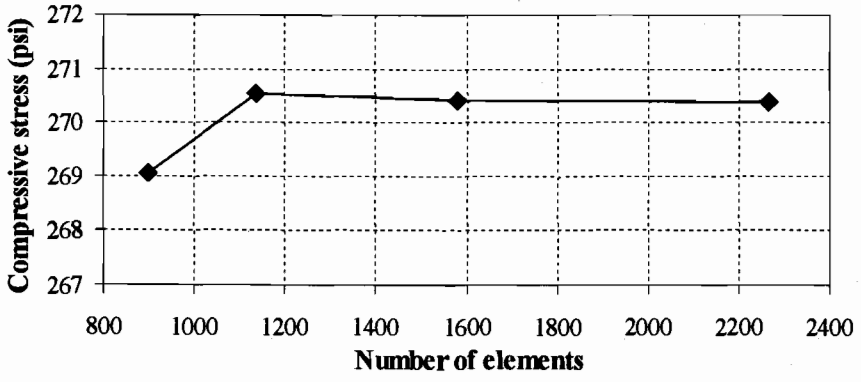

(b)

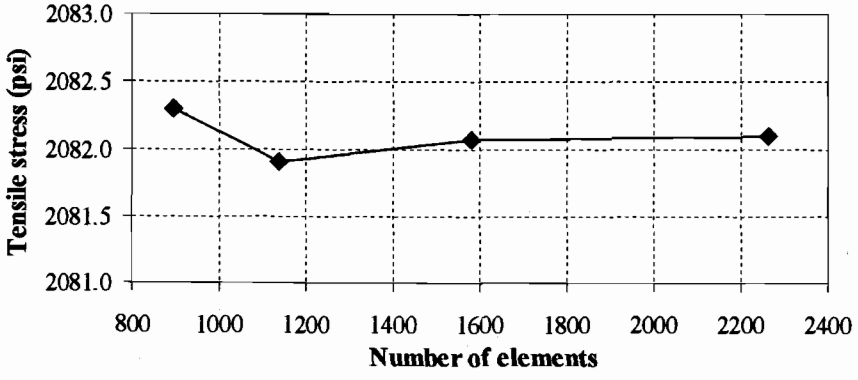

(c)

Figure 2.18: Results from Convergence Study: (a) Deflection at Midspan; (b) Compressive Stress in Concrete; (c) Tensile Stress in Main Steel Reinforcement

Figure 2.18 shows that the differences in the results are negligible when the number of elements increases from 1580 to 2264. Therefore, the 1580 element model was selected for the control beam model and used as the basis of the other three FRP strengthened beam models as well.

Figure 2.19 shows meshing for the control beam model. A finer mesh near the loading location is required in order to avoid problems of stress concentration.

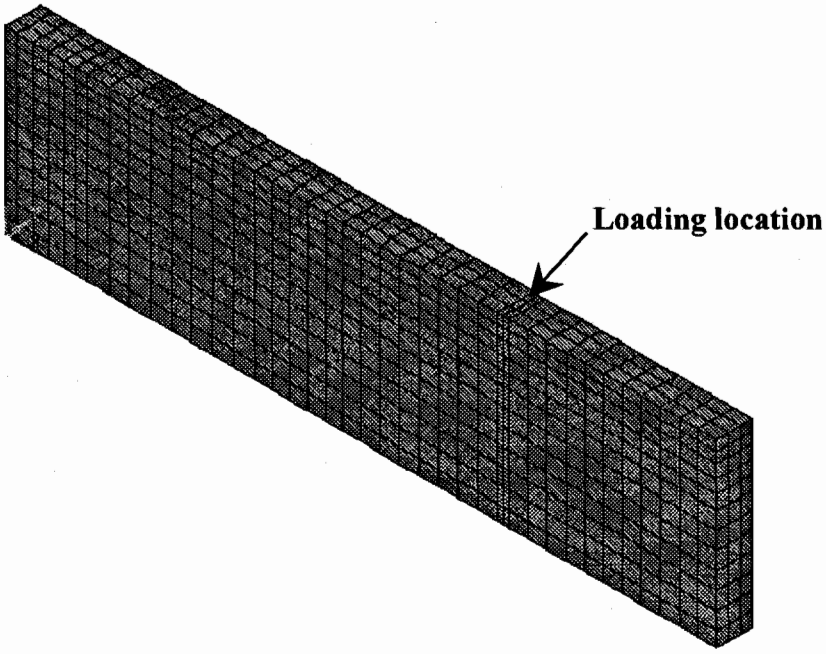

Figure 2.19: Meshing for a Quarter of Control Beam

FRP layered solid elements are connected to the surfaces of the concrete solid elements of the control beam as shown in Figure 2.15(b). The dimensions for the FRP reinforcing schemes are shown in Figure 2.17. Numbers of elements used in this study are summarized in Table 2.3.

Table 2.3: Numbers of Elements Used for Finite Element Models

Model	Number of elements				
	Concrete	Steel reinforcement	FRP composites	Steel plate	Total
Control beam	1404	164	-	12	1580
Flexural beam	1404	164	222	12	1802
Shear beam	1404	164	490	12	2070
Flexural/Shear beam	1404	164	1062	12	2642

2.3.3. Loading and Boundary Conditions

The four experimental beams were tested in third point bending as shown in Figure 2.20. The finite element models are loaded at the same locations as the experimental beams. In the experiment, the loading and support dimensions were measured to be approximately $2in. \times 8in.$ and $4in. \times 12in.$, respectively.

A quarter of the entire beam is used for the models in this study. Planes of symmetry are required at the cut faces. At a plane of symmetry, the displacement in the direction perpendicular to the plane must be equal to zero. Figure 2.21 shows loading and boundary conditions for a typical finite element model. Rollers are used to show the symmetry condition at the cut faces.

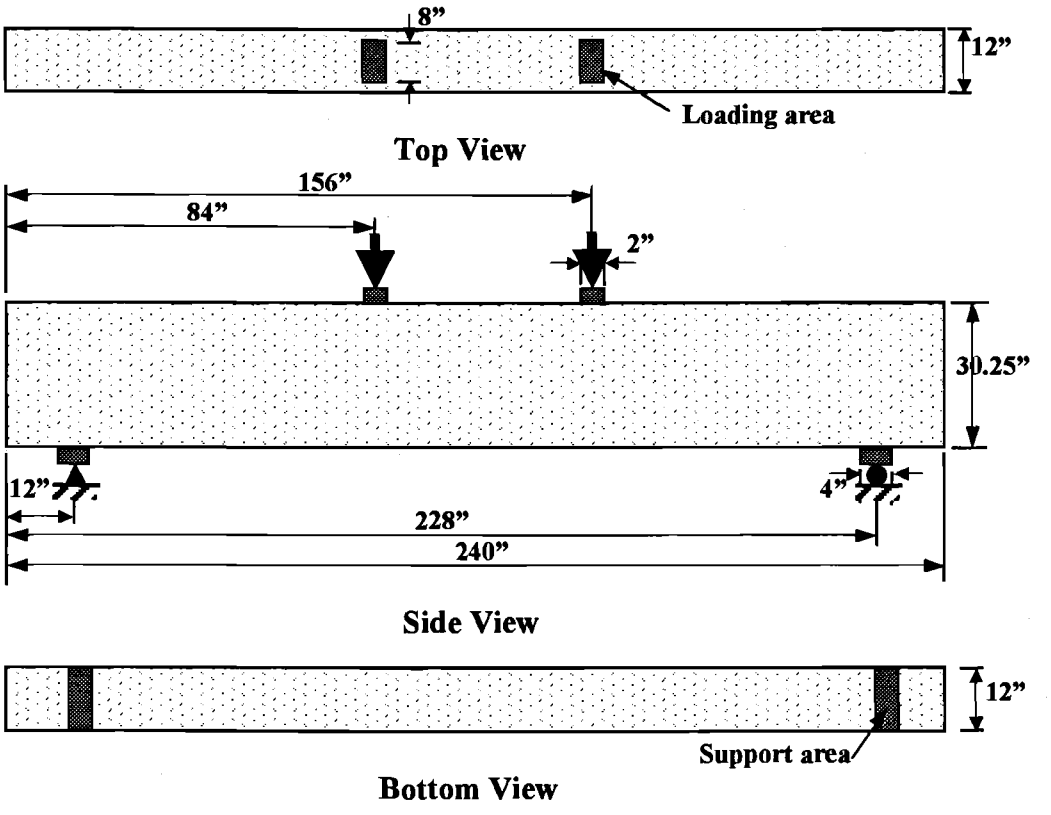

Figure 2.20: Loading and Support Locations (not to scale)
(McCurry and Kachlakev, 2000)

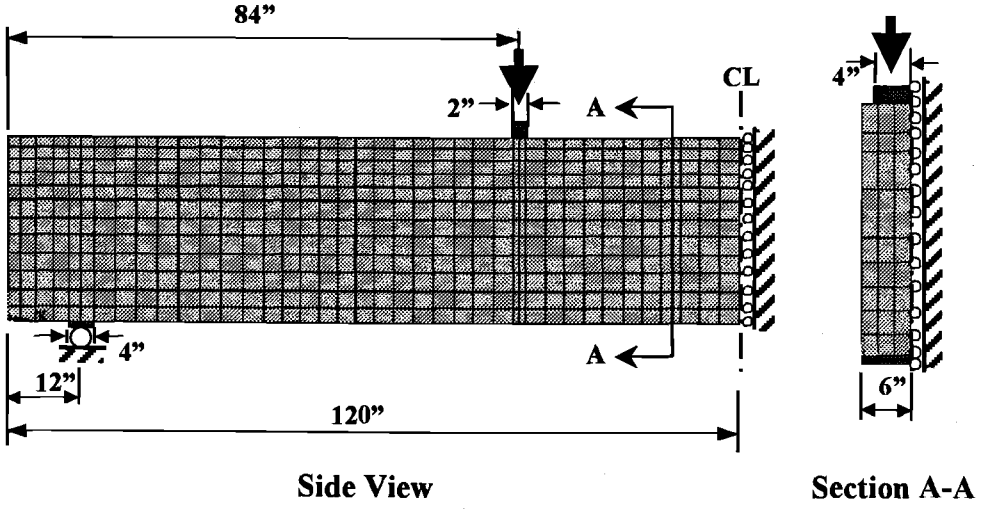

Figure 2.21: Loading and Boundary Conditions (not to scale)

Locations for the loading and supports on the experimental beams are shown in Figure 2.20. For the finite element models, each load is distributed over a small area as for the experimental beams. A one-inch thick steel plate, modeled using Solid45 elements, is added at the support location in order to avoid stress concentration problems. This provides a more even stress distribution over the support area. Moreover, a single line support is placed under the centerline of the steel plate to allow rotation of the plate. Figure 2.22 illustrates the steel plate at the support.

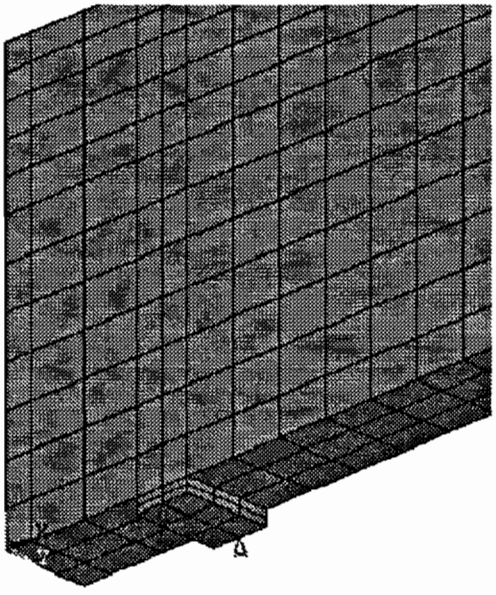

Figure 2.22: Steel Plate with Line Support

When the loaded beam starts to displace downward, rotation of the plate should be permitted. Excessive cracking of the concrete elements above the steel plate was found to develop if rotation of the steel plate is not permitted as shown in Figure 2.23(a).

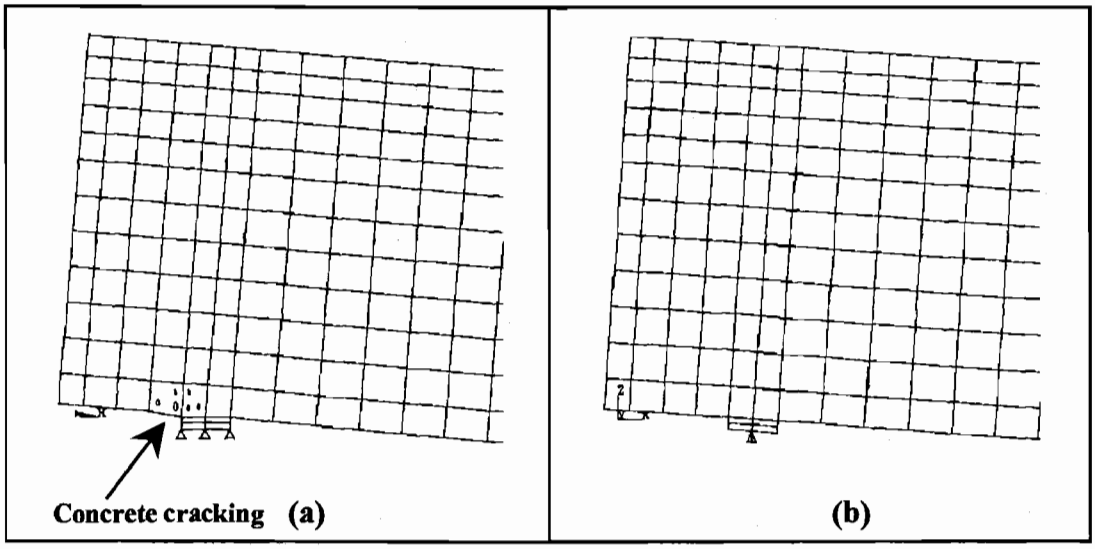

Figure 2.23: Displacements of Model: (a) Without Rotation of Steel Plate (b) With Rotation of Steel Plate

2.3.4. Nonlinear Solution

In nonlinear analysis, the total load applied to a finite element model is divided into a series of load increments called load steps. At the completion of each incremental solution, the stiffness matrix of the model is adjusted to reflect nonlinear changes in structural stiffness before proceeding to the next load increment. The ANSYS program (ANSYS 5.5: ANSYS, Inc., 1998) uses Newton-Raphson equilibrium iterations for updating the model stiffness.

Newton-Raphson equilibrium iterations provide convergence at the end of each load increment within tolerance limits. Figure 2.24 shows the use of the Newton-Raphson approach in a single degree of freedom nonlinear analysis.

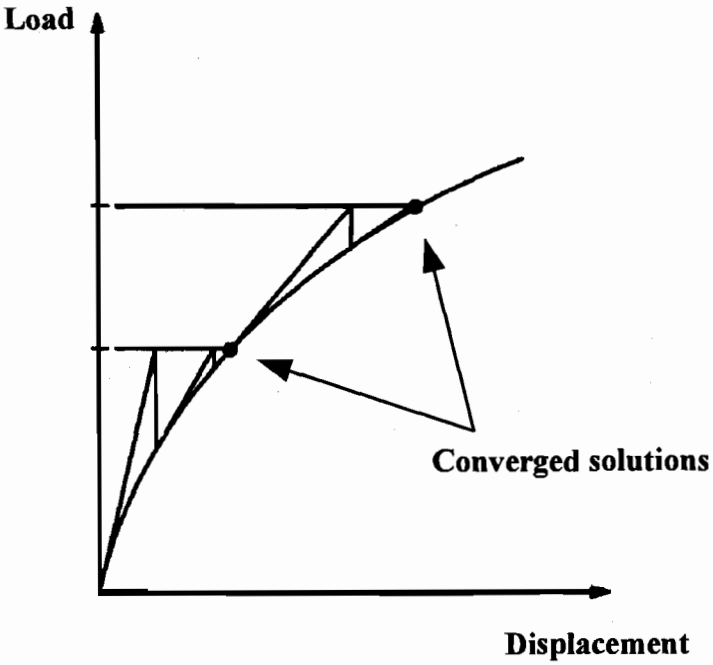

Figure 2.24: Newton-Raphson Iterative Solution (2 load increments) (ANSYS, 1998)

Prior to each solution, the Newton-Raphson approach assesses the out-of-balance load vector, which is the difference between the restoring forces (the loads corresponding to the element stresses) and the applied loads. Subsequently, the program carries out a linear solution, using the out-of-balance loads, and checks for convergence. If convergence criteria are not satisfied, the out-of-balance load vector is re-evaluated, the stiffness matrix is updated, and a new solution is attained. This iterative procedure continues until the problem converges (ANSYS, 1998).

In this study, for the reinforced concrete solid elements, convergence criteria were based on force and displacement convergence checking, and the convergence tolerance limits were initially selected by the ANSYS program. It was found that

convergence of solutions for the models was difficult to achieve due to the nonlinear behaviors of reinforced concrete. Therefore, the convergence tolerance limits were relaxed a maximum of 5 times the initially selected tolerance limits in order to obtain convergence of the solutions.

2.3.5. Load Stepping and Failure Definition for FE Models

For the nonlinear analysis, automatic time stepping in the ANSYS program predicts and controls load step sizes. Based on the previous solution history and the physics of the models, if the convergence behavior is smooth, automatic time stepping will increase the load increment up to a selected maximum load step size, whereas if the convergence behavior is difficult, automatic time stepping will bisect or cut back the load increment until it is equal to a selected minimum load step size. The maximum and minimum load step sizes are required for the automatic time stepping.

In this study, the convergence behavior of the models depends on behavior of the reinforced concrete. The flexural/shear strengthened beam model is used here as an example to demonstrate the load stepping. Figure 2.25 shows the load-deflection plot with reinforced concrete behaviors occurring in the beam model under loading.

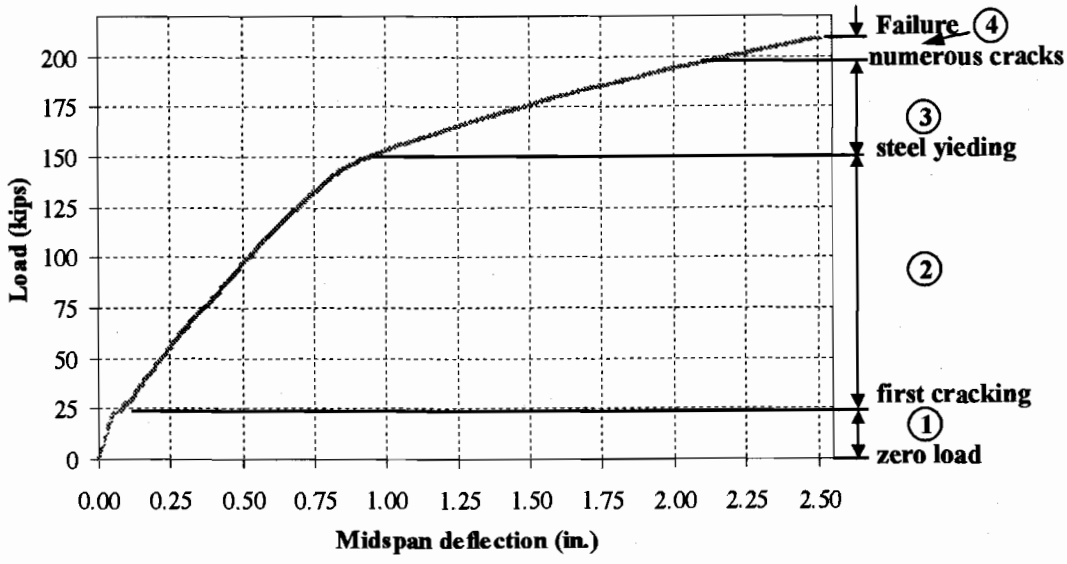

Figure 2.25: Reinforced Concrete Behavior in Flexural/Shear Strengthened Beam

Table 2.4 is a summary of the load step sizes used for the beam model. The load step sizes are adjusted depending upon the behavior occurring in the model.

Table 2.4: Summary of Load Step Sizes for Flexural/Shear Strengthened Beam Model

Reinforced concrete behavior	Load step sizes (lb)	
	Minimum	Maximum
1 Zero load – First cracking	1000	5000
2 First cracking – Steel yielding	2	75
3 Steel yielding – Numerous cracks	1	25
4 Numerous cracks – Failure	1	5

As shown in the table, the load step sizes do not need to be small in the linear range (region **1**). At the beginning of region **2**, cracking of the concrete starts to occur, so the loads are applied gradually with small load increments. A minimum load step size of 2 lb is defined for the automatic time stepping within this region. As first cracking occurs, the solution becomes difficult to converge. If a load applied on the model is not small enough, the automatic time stepping will bisect the load until it is equal to the minimum load step size. After the first cracking load, the solution becomes easier to converge, therefore the automatic time stepping increases the load increment up to the defined maximum load step size, which is 75 lb for this region. If the load step size is too large, the solution either needs a large number of iterations to converge, which increases computational time considerably, or diverges. In region **3**, the solution becomes more difficult to converge due to yielding of the steel. Therefore, the maximum load step size is reduced to 25 lb. A minimum load step size of 1 lb is defined to ensure that the solution will converge, even if a major crack occurs within this region. Last, for region **4**, a large number of cracks occur as the applied load increases. The maximum load step size is defined to be 5 lb, and a 1 lb load increment is specified for the minimum load step size for this region. For this study, a load step size of 1 lb is generally small enough to obtain converged solutions for the models.

Failure for each of the models is defined when the solution for a 1 lb load increment still does not converge. The program then gives a message specifying that the models have a significantly large deflection exceeding the displacement limitation of the ANSYS program.

3. RESULTS FROM FINITE ELEMENT ANALYSIS

Results from the ANSYS finite element analyses of the four full-scale beams are compared with the experimental data (McCurry and Kachlakev, 2000). Comparisons are made as follows: load-strain plots at selected locations; load-deflection plots at midspan; first cracking loads; loads at failure; and crack patterns at failure. Moreover, the evolutions of crack patterns, stress contours in the concrete for each beam model, and summaries of the maximum stresses occurring in the FRP composites for the finite element models are also presented. The data from the finite element analyses are collected at the same locations as for the experimental beams.

3.1. Load-Strain Plots

Conventional 2.36 in. long resistive strain gauges were placed throughout the experimental beams. The strain gauges were placed on concrete surfaces, FRP surfaces, and inside the beams on the main steel reinforcing bars at midspan. The locations of selected strain gauges used to compare with the finite element results are shown in Figure 3.1.

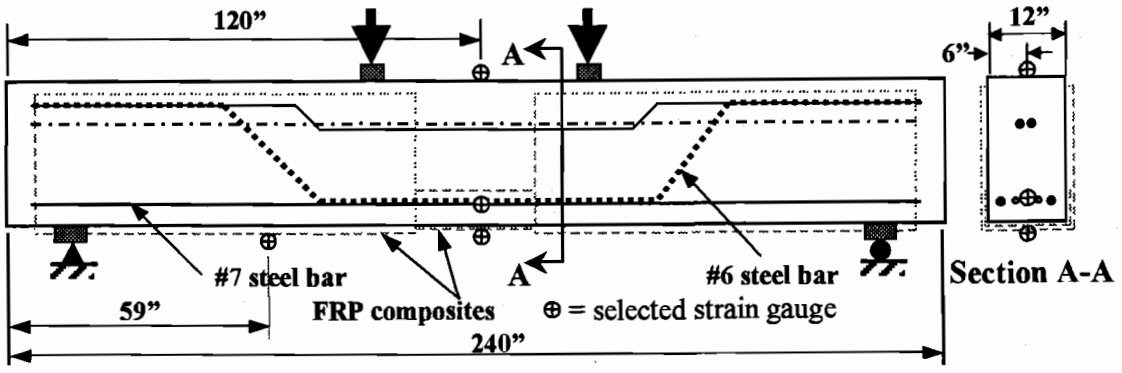

Figure 3.1: Selected Strain Gauge Locations (not to scale)

3.1.1. Tensile Strain in Main Steel Reinforcing

For the control, flexural strengthened, and shear strengthened beams, experimental strain data (McCurry and Kachlakev, 2000) were collected from strain gauges on the No.7 steel rebars at the midspan; for the flexural/shear strengthened beam, strain data were collected from a strain gauge on the No.6 steel rebar at midspan. Locations of the strain gauges are shown in Figure 3.1. Comparisons of the load-tensile strain plots from the finite element analyses and the experimental data for the main steel reinforcing at midspan for each beam are shown in Figures 3.2, 3.3, 3.4, and 3.5. Note that the vertical axis shown in the figures represents the total load on the beams.

Figure 3.2 shows that before the strain reverses in the experimental control beam, the trends of the finite element and the experimental results are similar. Especially in the linear range the strains from the finite element analysis correlate well with those from the experimental data. The finite element model then has lower strains than the experimental beam at the same load. The reversing strain in the experimental

beam is possibly a local effect caused by the major cracks, which take place close to the midspan. This behavior does not occur in the finite element model with a smeared cracking approach. Last, the steel at midspan in the finite element model has not yielded at failure for the control beam model, and this is also true for the steel in the experimental beam.

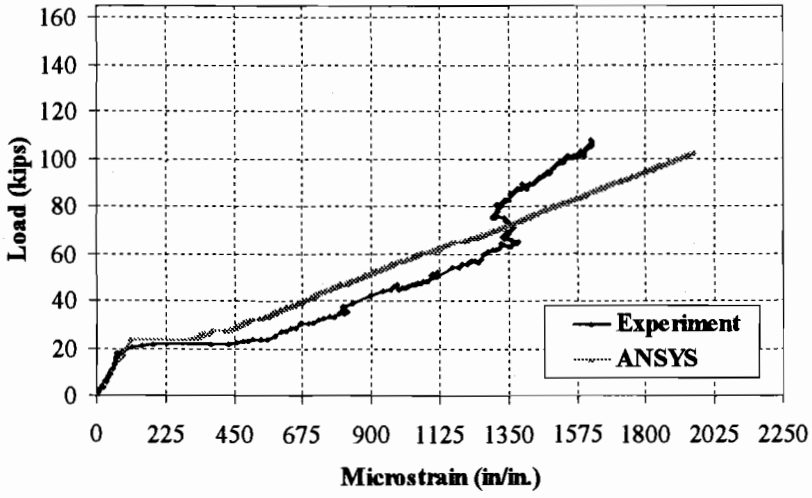

Figure 3.2: Load-Tensile Strain Plot for #7 Steel Rebar in Control Beam

Figure 3.3 shows good agreement for the strains from the finite element analysis and the experimental results for the flexural strengthened beam up to 110 kips. The finite element model for the flexural strengthened beam then has higher strains than the experimental beam at the same load. At 110 kips, the strain in the flexural strengthened beam reverses, as for the experimental control beam. The steel yields at an applied load of 138 kips for the model, whereas the steel in the experimental beam has not quite yielded at failure of the beam.

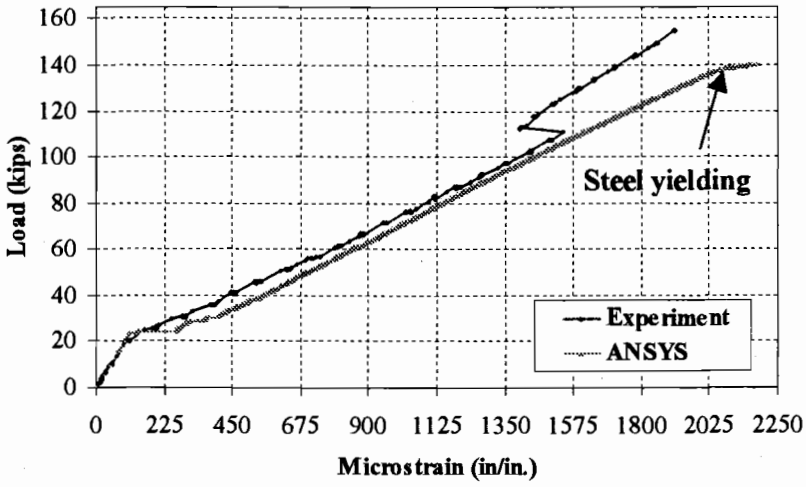

Figure 3.3: Load-Tensile Strain Plot for #7 Steel Rebar in Flexural Strengthened Beam

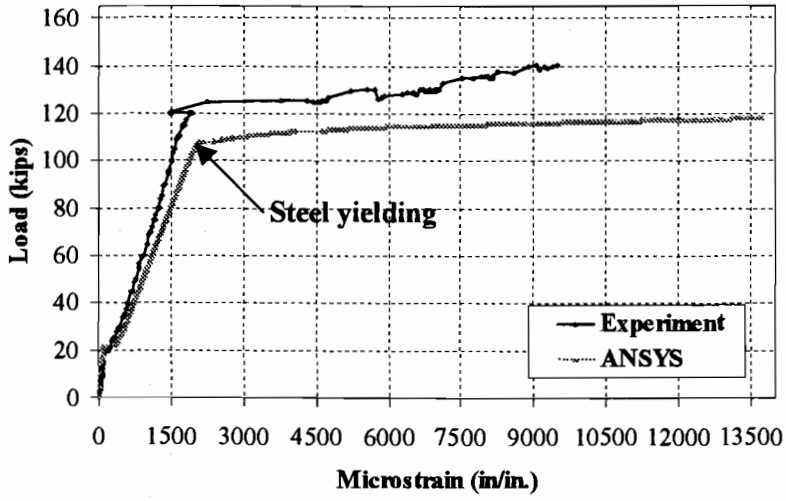

Figure 3.4: Load-Tensile Strain Plot for #7 Steel Rebar in Shear Strengthened Beam

Figure 3.4 shows that the strain data from the finite element analysis and the experimental data for the shear strengthened beam have similar trends. Similar to the

plots of strains in the steel for the flexural strengthened beam, the finite element model for the shear strengthened beam has higher strains than the experimental beam at the same load. The steel in the finite element model yields at an applied load of 108 kips, whereas the steel in the experimental beam yields at approximately 126 kips, a difference of 14%.

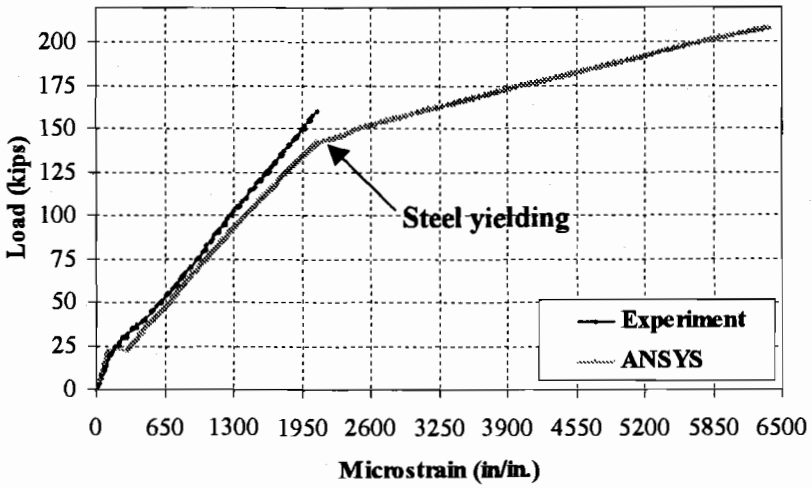

Figure 3.5: Load-Tensile Strain Plot for #6 Steel Rebar in Flexural/Shear Strengthened Beam (Experimental beam did not fail)

Figure 3.5 shows that the strains calculated by ANSYS agree well with those from the experimental results for the flexural/shear strengthened beam. Similar to the control, flexural and shear strengthened beams, the strains for the flexural/shear strengthened beam from the finite element analysis correlate well with those from the experimental data in the linear range. The comparison ends at the maximum experimental applied load of 160 kips due to limitations in the capacity of the testing

machine. For the flexural/shear strengthened beam, the steel in the beam model yields before failure, which supports calculations for the experiment (McCurry and Kachlakev, 2000).

In general, the plots of load versus tensile strains in the main steel reinforcing from the finite element analyses have similar trends to those from the experimental results. In the linear range, the strains calculated by the finite element program are nearly the same as those measured for the experimental beams. However, after cracking of the concrete, an apparent inconsistency occurs in the comparisons of the results from the finite element analyses and the experimental data. For the control beam, ANSYS predicts that the strains occurring in the steel are lower than those in the experimental beam, while the strains occurring for the other three models are higher than those in the experimental beams.

In a reinforced concrete beam, at a sufficiently high load, the concrete fails to resist tensile stresses only where the cracks are located as shown in Figure 3.6(a). Between the cracks, the concrete resists moderate amounts of tension introduced by bond stresses acting along the interface in the direction shown in Figure 3.6(b). This reduces the tensile force in the steel, as illustrated by Figure 3.6(d) (Nilson, 1997).

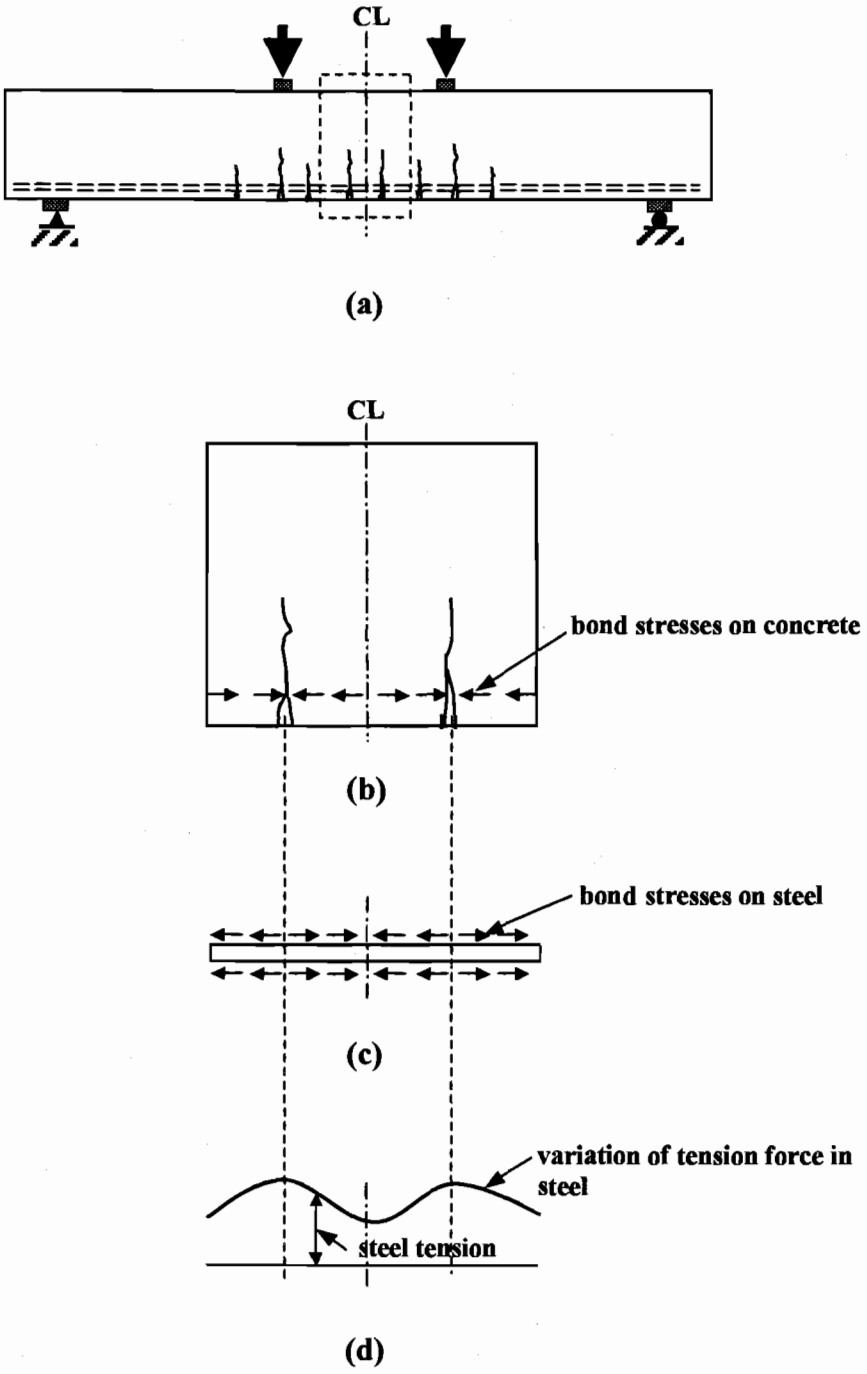

Figure 3.6: Variation of Steel Force for Reinforced Concrete Beam: (a) Typical Actual Cracking; (b) Cracked Concrete Section; (c) Bond Stresses Acting on Reinforcing Bar; (d) Variation of Tensile Force in Steel (Nilson, 1997)

Generally, strains in the steel reinforcement for the finite element models were higher than those for the experimental beams after cracking of the concrete. Figure 3.7 shows the average steel force in the finite element models. In the smeared cracking approach, the smeared cracks spread over the region where the principal tensile stresses in the concrete elements exceed the ultimate tensile strength as shown in Figures 3.7(a) and 3.7(b) rather than having discrete cracks. The stiffness of the cracked concrete elements in the finite element model reduces to zero, so they cannot resist tension. Therefore, the tension in the steel elements for the finite element model does not vary as occurs in the real beam. The tensile force in the steel elements is constant across the elements (Figure 3.7(c)). For this reason, strains calculated from the finite element analyses could be higher than those from the experimental results. This could also explain the difference in the steel yielding loads between the finite element and the experimental results for the flexural and shear strengthened beams as shown in Figures 3.3 and 3.4, respectively.

The inconsistency in the comparisons of the strains between the control beam and the other three FRP strengthened beams may be also explained by the variation of the steel force in the actual beams. For the experimental control beam, a crack may occur very close to the strain gauge, and could create additional tensile strains for the control beam. For the finite element model, the tension force and strain in the steel elements are constant across each element as shown in Figure 3.7(c).

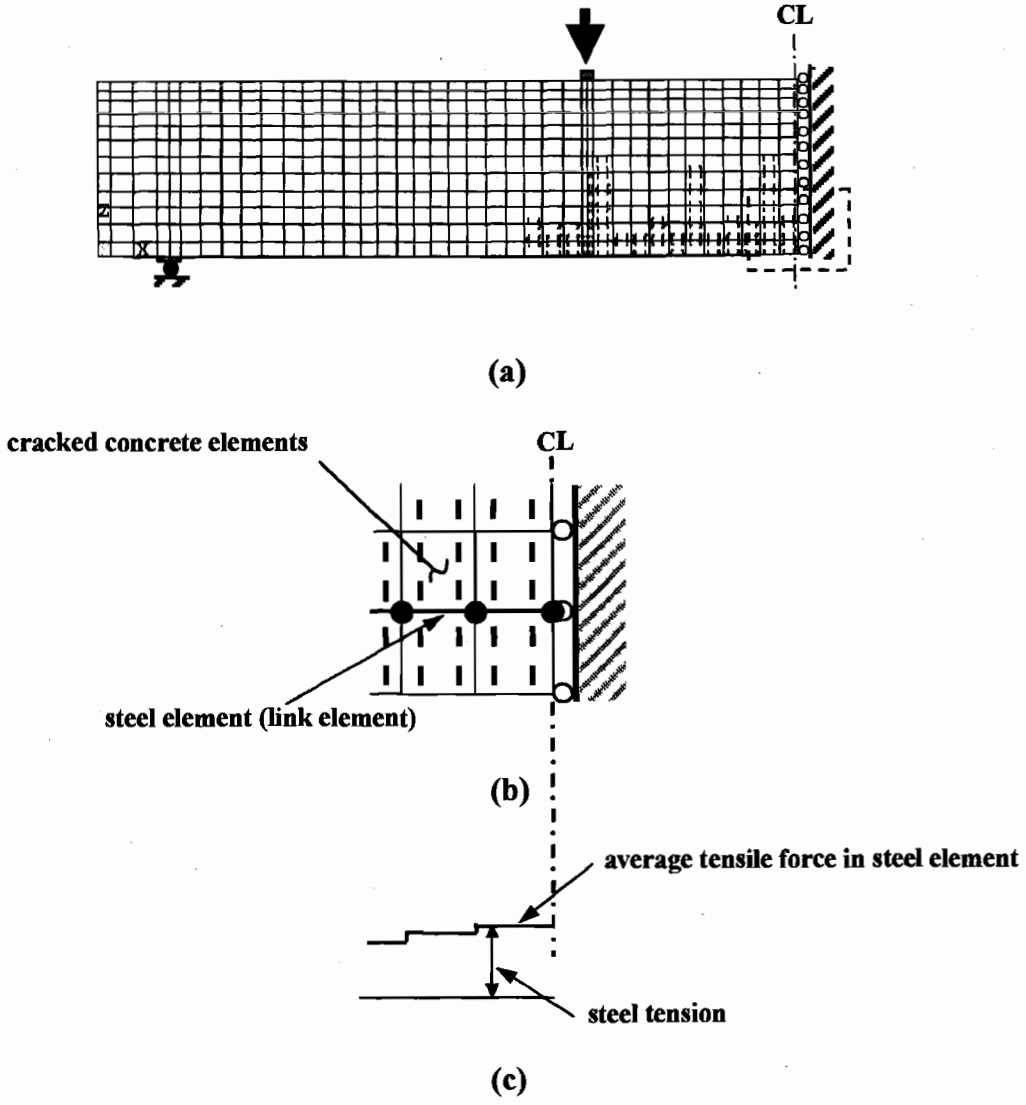

Figure 3.7: Average of Steel Force for Finite Element Models: (a) Typical Smeared Cracking; (b) Cracked Concrete and Steel Rebar Elements; (c) Average Tensile Force in Steel Element

3.1.2. Tensile Strain in FRP Composites

The locations of the strain gauges on the FRP reinforcing are shown in Figure 3.1. For the flexural and flexural/shear strengthened beams, experimental strain data were collected at midspan and center of the bottom of the beam on the surfaces of the

CFRP composites, whereas for the shear strengthened beam the strains were measured on the surface of the GFRP composite at a location 59 inches from the end of the beam and at the center of the width of the beam. Comparisons of the load-tensile strain plots from the finite element analyses and the experimental data for the FRP strengthened beams are shown in Figures 3.8, 3.9,and 3.10.

Figure 3.8 shows good agreement for the CFRP strains from the finite element analysis and the experimental results for the flexural strengthened beam. The finite element model for the flexural strengthened beam has higher strains than the experimental beam at the same load. Recall that the strains in the steel from the finite element analysis are higher than those from the experimental data for the flexural strengthened beam. As the strains in the steel are higher, the strains in the CFRP reinforcing could also be higher for similar reasons.

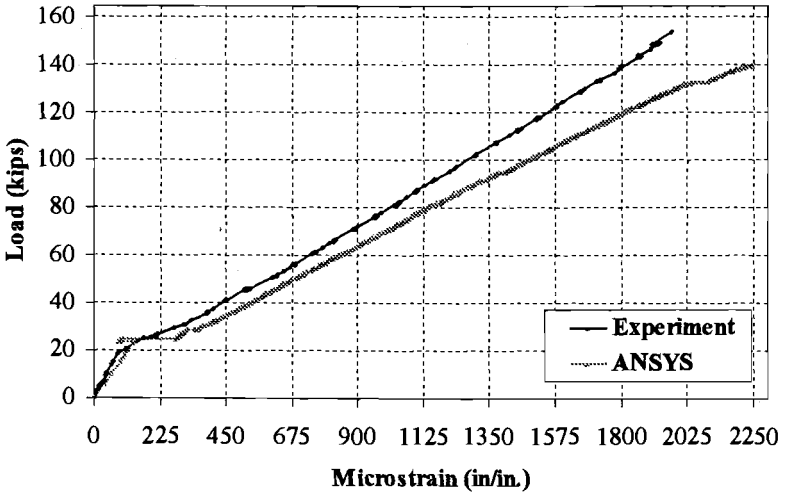

Figure 3.8: Load-Tensile Strain Plot for CFRP Composite in Flexural Strengthened Beam

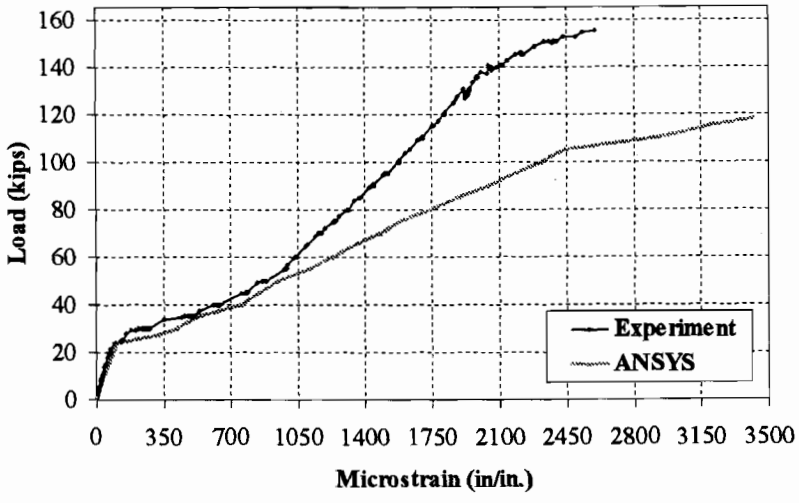

Figure 3.9: Load-Tensile Strain Plot for GFRP Composite in Shear Strengthened Beam

Figure 3.9 shows that the GFRP strain data from the finite element analysis and the experimental data for the shear strengthened beam have similar trends initially. Similar to the flexural strengthened beam, the strains calculated by the finite element analysis for the shear strengthened beam are higher than those for the experimental beam at the same load. However, after 50 kips the difference in strains between the finite element model and the experimental beam increases more dramatically.

Figure 3.10 shows that the CFRP strain data from the finite element analysis and the experimental data for the flexural/shear strengthened beam have good agreement up to 160 kips. The CFRP strains in the finite element model are again higher than those in the experimental beam, possibly for similar reasons as for the steel strains.

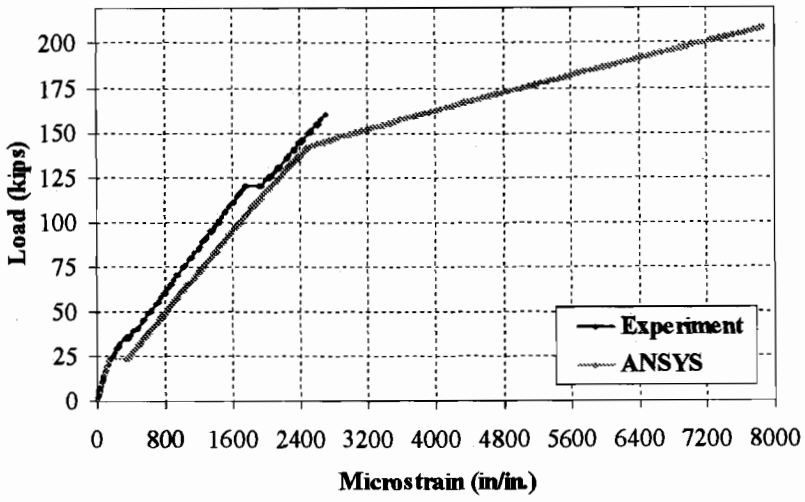

Figure 3.10: Load-Tensile Strain Plot for CFRP Composite in Flexural/Shear Strengthened Beam (Experimental beam did not fail)

3.1.3. Compressive Strain in Concrete

The load-compressive strain plots in concrete collected from the experiment are compared with results from the finite element analysis. A strain gauge was placed at midspan and center of the top face for all four beams as shown in Figure 3.1. Figures 3.11, 3.12, 3.13, and 3.14 are comparisons of the load-compressive strain plots for the concrete for all four beams.

Figure 3.11 shows that the load-compressive strain plots for the concrete from the finite element analysis and the experimental data have excellent agreement for the control beam. Figure 3.12 shows that the load-compressive strain plots for the flexural strengthened beam have a similar trend, however strains in the concrete calculated by ANSYS are higher than those from the experimental results at the same load.

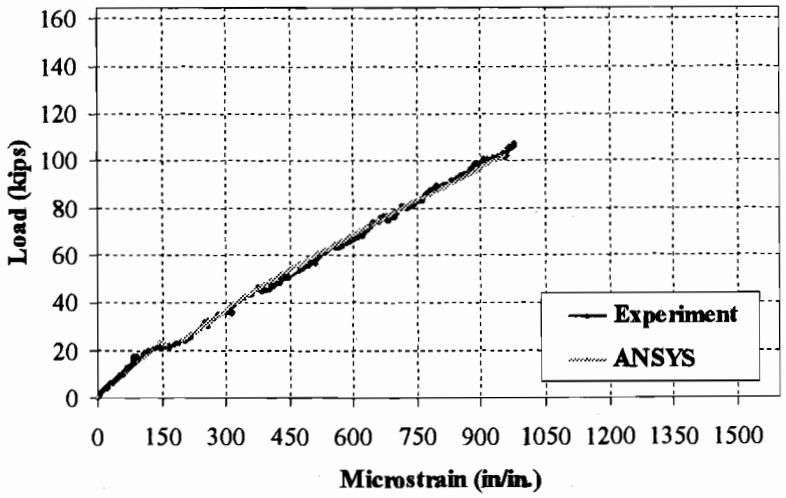

Figure 3.11: Load-Compressive Strain Plot for Concrete in Control Beam

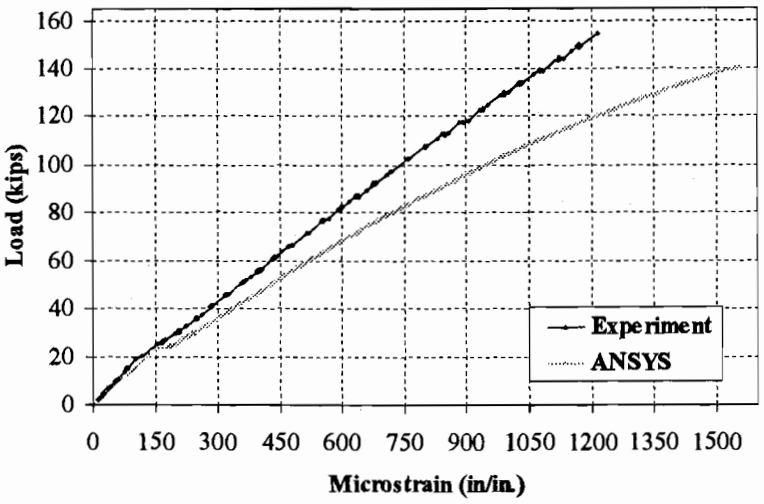

Figure 3.12: Load-Compressive Strain Plot for Concrete in Flexural Strengthened Beam

Figure 3.13 shows the load-compressive strain plots for the shear strengthened beam. For applied loads from 0 to 105 kips, the load-strain plots for the shear

strengthened beam from the finite element and experimental results do not correlate well. As shown in the figure, the experimental beam shows nonlinear behavior. This behavior should not happen at this load level. Either erroneous test data or local material imperfections may cause the behavior. Cracks occurring at the interfaces between the cement and aggregate due to their differences in elastic modulus, thermal coefficient, and response to change in moisture content when the concrete is hardened could be the source of the local material imperfections. At about 110 kips, large strains occur for the finite element model, whereas at a load of 120 kips similar behavior takes place for the experimental beam. These loads are close to the yielding loads of the steel as shown in Figure 3.4. The yielding of the steel explains the large concrete strains.

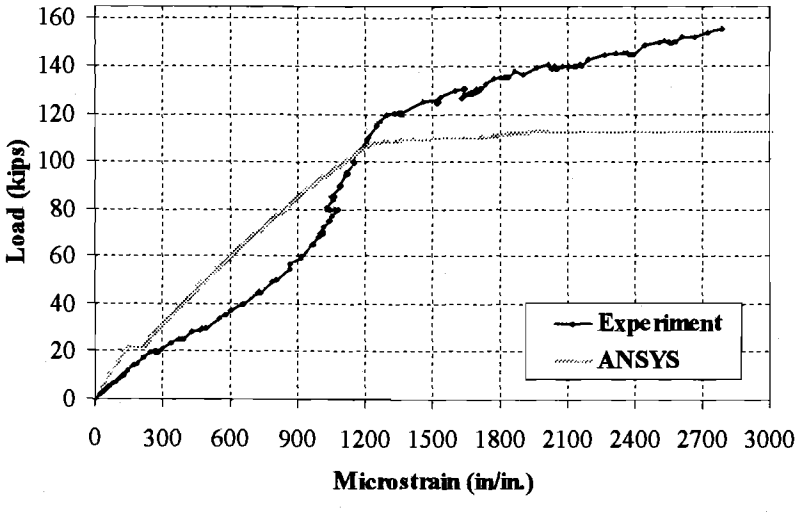

Figure 3.13: Load-Compressive Strain Plot for Concrete in Shear Strengthened Beam

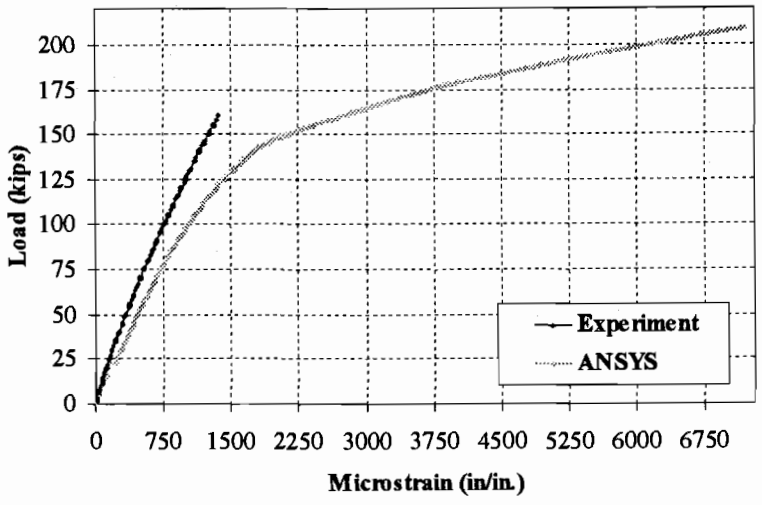

Figure 3.14: Load-Compressive Strain Plot for Concrete in Flexural/Shear Strengthened Beam (Experimental beam did not fail)

Up to the maximum applied load of 160 kips in the experimental beam, Figure 3.14 shows the finite element model having larger strains at the same load compared to the experimental beams.

In general, the strains in the concrete from the finite element analyses are higher than those from the experimental data. It is possible that the material properties of the concrete obtained from the experiment (pulse velocity measurements) may be inaccurate.

3.2. Load-Deflection Plots

Direct current displacement transducers (DCDTs) were used to measure deflections for the experimental beams at midspan at the center of the bottom face of the beams. For ANSYS, deflections are measured at the same location as for the

experimental beams. Figures 3.15, 3.16, 3.17, and 3.18 show the load-deflection plots from the finite element analyses and the experimental results for all four beams.

Figure 3.15 shows that the load-deflection plot for the control beam from the finite element analysis agrees well with that from the experimental data. In the linear range, the load-deflection plot from the finite element analysis is stiffer than that from the experimental results by approximately 66%. The first cracking load for the finite element analysis is 23.5 kips, which is higher than the load of 17.6 kips from the experimental results by 34%. After first cracking, the finite element model is again stiffer than the experimental beam by approximately 28%. At 90 kips, for the finite element control beam model, yielding of the steel No.7 occurs at a location approximately 70 inches from the end of the beam, resulting in the decreased stiffness of the model. Last, the final load of 102 kips from the model is lower than the ultimate load of 107 kips from the experimental data by only 5%.

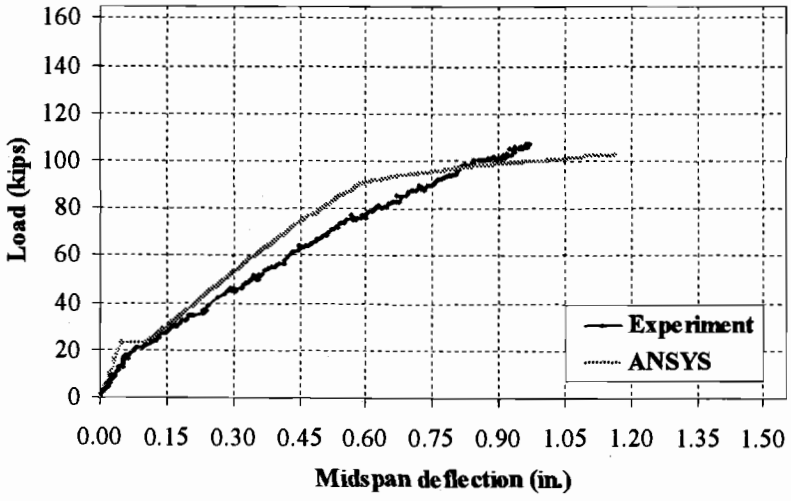

Figure 3.15: Load-Deflection Plot for Control Beam

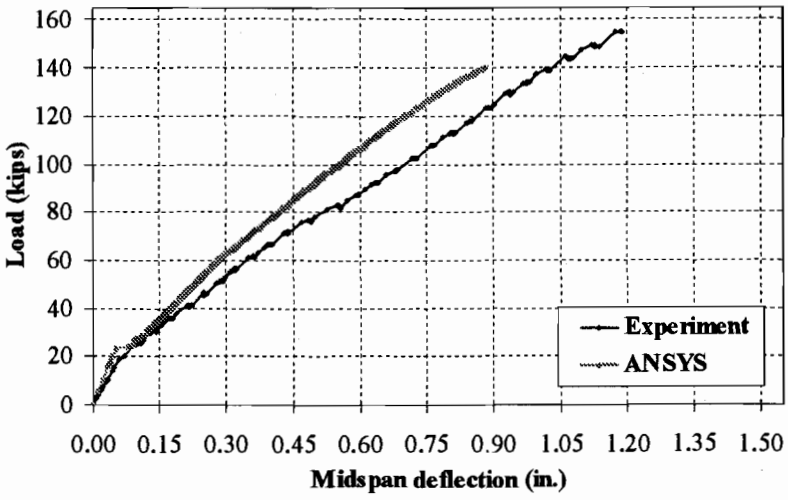

Figure 3.16: Load-Deflection Plot for Flexural Strengthened Beam

Figure 3.16 shows that the load-deflection plots for the flexural strengthened beam from the experimental data and the finite element analysis are in reasonably good agreement. Similar to the control beam, the finite element model is stiffer than the experimental beam in the linear range by approximately 55%. The finite element model cracks at 23.4 kips, which is higher than the experimental beam cracking load of 21.7 kips by 8%. After first cracking, the two plots have a similar trend, however, the finite element model is again stiffer than the experimental beam by approximately 27%. The final load for the model is 140 kips, which is less than the ultimate load of 155 kips for the experimental beam by 10%.

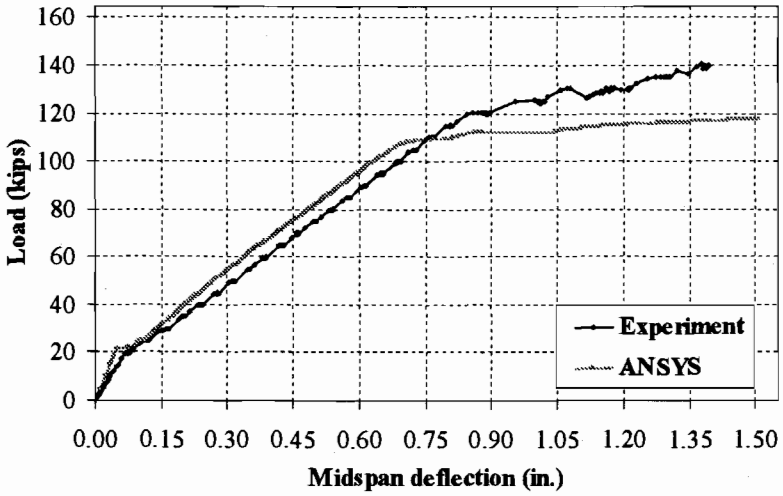

Figure 3.17: Load-Deflection Plot for Shear Strengthened Beam

As shown in Figure 3.17, the two load-deflection plots for the shear strengthened beam correlate well with each other. The finite element model is stiffer than the experimental beam in the linear range by approximately 52%. The first cracking load for the finite element model is 21.6 kips, which is higher than the load of 19.7 kips from the experimental results by 10%. After first cracking, the finite element model and the experimental beam have almost the same stiffness. However, large deflections begin to occur in the finite element model at a load of 110 kips, whereas the same behavior in the experimental beam is observed at about 120 kips. It is evident that the yielding of the steel reinforcement creates the large deflections. The final load for the finite element model is 118 kips, which is less than the ultimate load of 155 kips for the experimental beam by 24%.

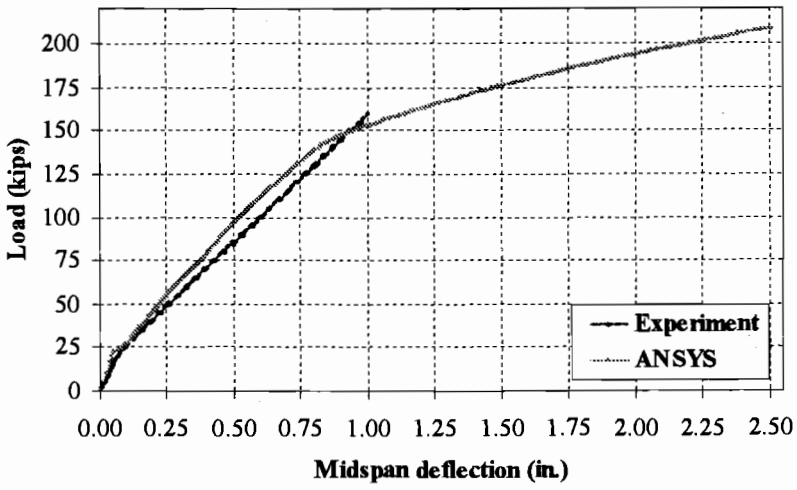

Figure 3.18: Load-Deflection Plot for Flexural/Shear Strengthened Beam
(Experimental beam did not fail)

As shown in Figure 3.18, the two load-deflection plots for the flexural/shear strengthened beam are compared up to a load of 160 kips, since experimental data are available only up to this point. The load-deflection plot from the finite element analysis agrees well with the experimental data. In the linear range, the load-deflection plot from the finite element analysis is slightly stiffer than that from the experimental results by about 12%. The first cracking load levels from the finite element analysis and the experimental results are 22.9 kips and 21.6 kips, respectively, a difference of 6%. After cracking, the stiffness for the finite element model is slightly higher than the experimental data by approximately 14%. Above a load of 145 kips, the stiffness of the finite element model reduces due to the yielding of the steel reinforcement in the beam model, and the final load is 209 kips.

In general, the load-deflection plots for all four beams from the finite element analyses agree quite well with the experimental data. For the four beams, the finite element load-deflection plots in the linear range are stiffer than the experimental plots by 12%-66%. The first cracking loads for all four models from the finite element analyses are higher than those from the experimental results by 6%-34%. After first cracking, the stiffness of the finite element models is again higher than that of the experimental beams by 14%-28%. There are several effects that may cause the higher stiffnesses in the finite element models. First, microcracks are present in the concrete for the experimental beams, and could be produced by drying shrinkage in the concrete and/or handling of the beams. On the other hand, the finite element models do not include the microcracks. The microcracks reduce the stiffness of the experimental beams. Next, perfect bond between the concrete and steel reinforcing is assumed in the finite element analyses, but the assumption would not be true for the experimental beams. As bond slip occurs, the composite action between the concrete and steel reinforcing is lost. Thus, the overall stiffness of the experimental beams is expected to be lower than for the finite element models (which generally impose additional constraints on behavior).

A combined load-deflection plot is used to show differences in behaviors for the four beams. Figure 3.19 illustrates the load-deflection plots for the four experimental beams, whereas Figure 3.20 shows the plots for the four finite element models.

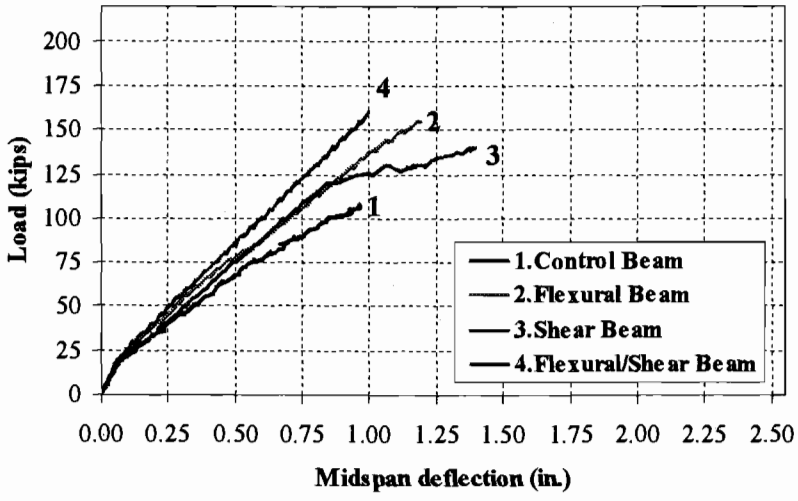

Figure 3.19: Load-Deflection Summary for Experimental Beams
(Beam No.4 did not fail) (Kachlakev and McCurry, 2000)

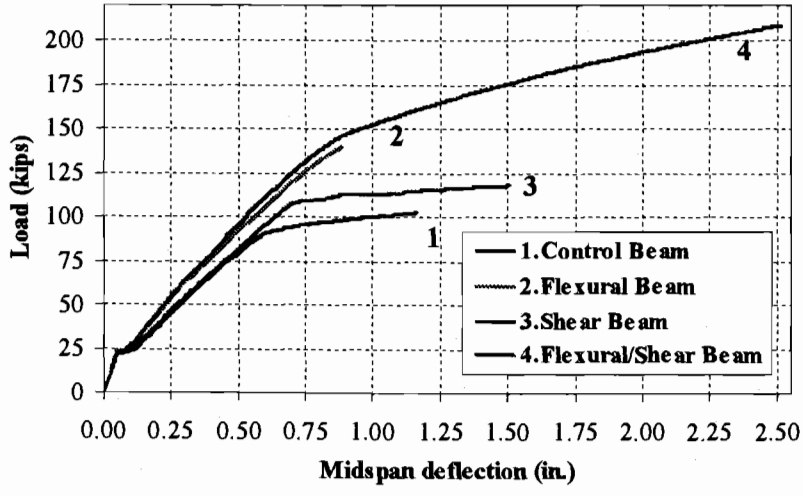

Figure 3.20: Load-Deflection Summary for All ANSYS Finite Element Models

The load-deflection plots from the finite element analyses and the experimental data both show that the stiffnesses of the beams before and after applying FRP strengthening are approximately the same in the linear range. After first cracking, the stiffnesses of the FRP strengthened beams from the finite element analyses are higher than for the control beam, which is consistent with the experimental results.

For the load-carrying capacity of the beams, the finite element models have the same sequence as for the experimental beams. For the finite element models, the flexural, shear, and flexural/shear strengthened beams have higher load carrying capacities than the control beam by 37%, 16%, and 105%, respectively, whereas the experimental FRP strengthened beams have capacities greater than the control beam by 45%, 45%, and 104%, respectively. Note that the capacity of the experimental flexural/shear strengthened beam was estimated from hand calculations (Kachlakev and McCurry, 2000).

3.3. First Cracking Loads

The first cracking load from the finite element analysis is the load step where the first signs of cracking occur for concrete in the model. Loads at first cracking from the model and the experimental results are compared in Table 3.1.

Table 3.1: Comparisons Between Experimental and ANSYS First Cracking Loads

Beam	First cracking load (kips)		%Difference
	Experiment*	ANSYS	
Control beam	17.6	23.5	34
Flexural beam	21.7	23.4	7.8
Shear beam	19.7	21.6	9.6
Flexural/Shear beam	21.6	22.9	6.0

*(McCurry and Kachlakev, 2000)

The first cracking loads from the finite element analyses and the experimental data are comparable, but the first cracking loads from ANSYS are generally somewhat higher as seen in Table 3.1. This is possibly due to the relative homogeneity of the finite element models when compared to the relative heterogeneity of the experimental beams that contain a number of microcracks. The finite element results also support the experimental observation that after applying the FRP composites, the FRP reinforcing scheme for the shear strengthened beam results in the lowest first cracking load when compared to the other two FRP strengthened beams.

3.4. Evolution of Crack Patterns

In ANSYS, outputs, i.e. stresses and strains, are calculated at integration points of the concrete solid elements. Figure 3.21 shows integration points in a concrete solid element. A cracking sign represented by a circle appears when a principal tensile stress

exceeds the ultimate tensile strength of the concrete. The cracking sign appears perpendicular to the direction of the principal stress as illustrated in Figure 3.22.

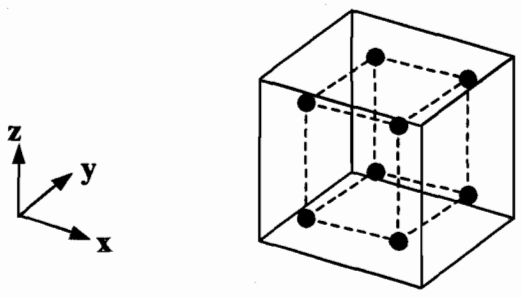

Figure 3.21: Integration Points in Concrete Solid Element (ANSYS, 1998)

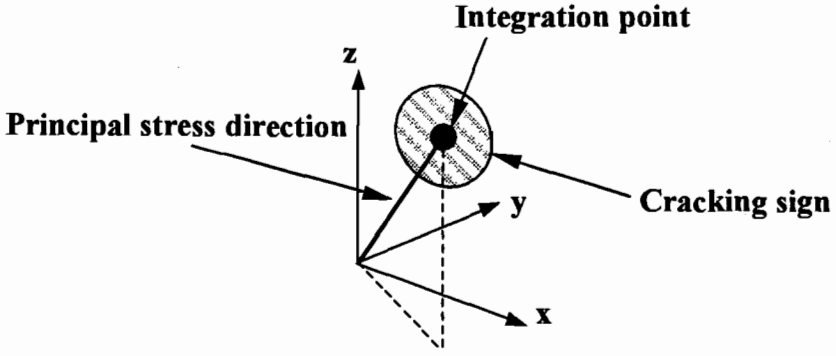

Figure 3.22: Cracking Sign (ANSYS, 1998)

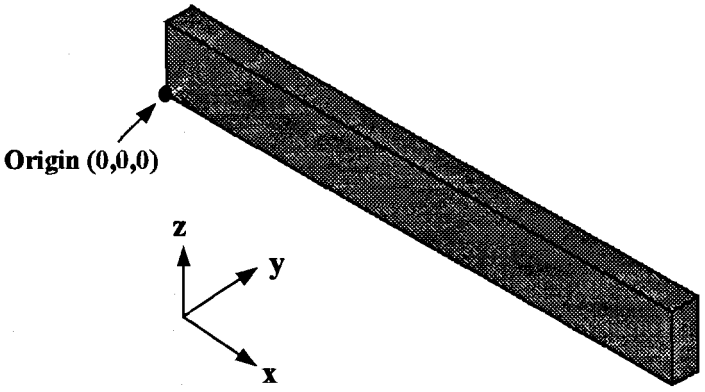

Figure 3.23: Coordinate System for Finite Element Models

Figure 3.23 shows the coordinate axes used in this finite element modeling study, where x, y, and z correspond to the length, width, and height directions for the beams, respectively. Figure 3.24 shows typical cracking signs in an ANSYS model. A side face of a quarter beam model is used to demonstrate. As shown in Figure 3.24(a), at midspan and at the bottom of the beam, principal tensile stresses occur mostly in the x direction (longitudinally). When the principal stresses exceed the ultimate tensile strength of the concrete, circles as cracking signs appear perpendicular to the principal stresses in the x direction. Therefore the cracking signs shown in the figure appear as vertical straight lines occurring at the integration points of the concrete solid elements. Hereafter, these will be referred to as flexural cracks.

Figure 3.24(b) shows the type of cracking signs observed for concrete elements underneath the loading locations. For a concrete structure subjected to uniaxial compression, cracks propagate primarily parallel to the direction of the applied compressive load, since the cracks result from tensile strains developed due to

Poisson's effect (Mindess and Young, 1981; Shah et al., 1995). Similar behavior is seen in the finite element analysis. Loads in the z direction result in tensile strains in the y direction by Poisson's effect. Thus, circles appear perpendicular to the principal tensile strains in the y direction at integration points in the concrete elements near the loading location. These will be referred to as compressive cracks.

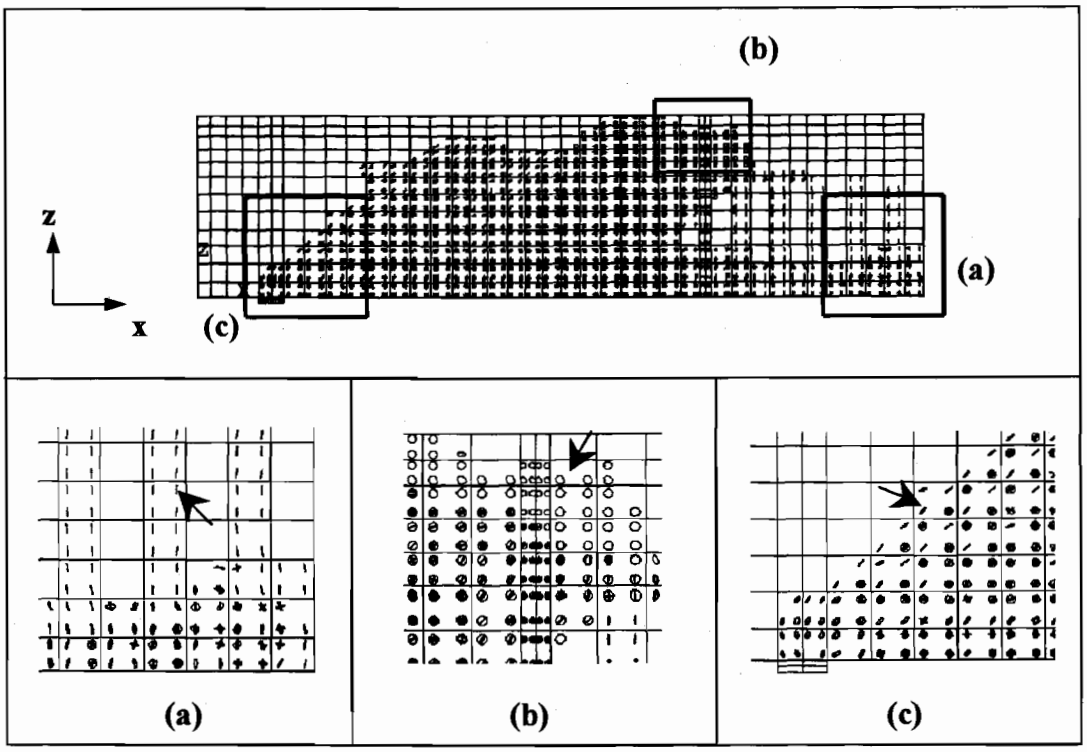

Figure 3.24: Typical Cracking Signs Occurring in Finite Element Models: (a) Flexural Cracks; (b) Compressive Cracks; (c) Diagonal Tensile Cracks

Figure 3.24(c) shows cracking signs where both normal and shear stresses act on concrete elements. By using transformation equations, directions and magnitudes of the

principal stresses can be obtained (Gere and Timoshenko, 1997). At the location shown in the figure, normal tensile stresses generally develop in the x direction and shear stresses occur in the xz plane. Consequently, the direction of tensile principal stresses becomes inclined from the horizontal. Once the principal tensile stresses exceed the ultimate tensile strength of the concrete, inclined circles appearing as straight lines perpendicular to the directions of the principal stresses appear at integration points of the concrete elements. Hereafter, these will be referred to as diagonal tensile cracks.

The ANSYS program records a crack pattern at each applied load step. Figure 3.25 shows evolutions of crack patterns developing for each beam. In general, flexural cracks occur early at midspan. When applied loads increase, vertical flexural cracks spread horizontally from the midspan to the support. At a higher applied load, diagonal tensile cracks appear. Increasing applied loads induces additional diagonal and flexural cracks. Finally, compressive cracks appear at nearly the last applied load steps. The cracks appear underneath the loading location on the control and flexural strengthened beam models. For the shear strengthened beam model, there are no compressive cracks underneath the loading location. On the flexural/shear strengthened beam model, significant cracks appear at the top of the beam. The appearance of the cracks defines the failure mode for the beams, which will be discussed in the failure crack pattern section of this thesis.

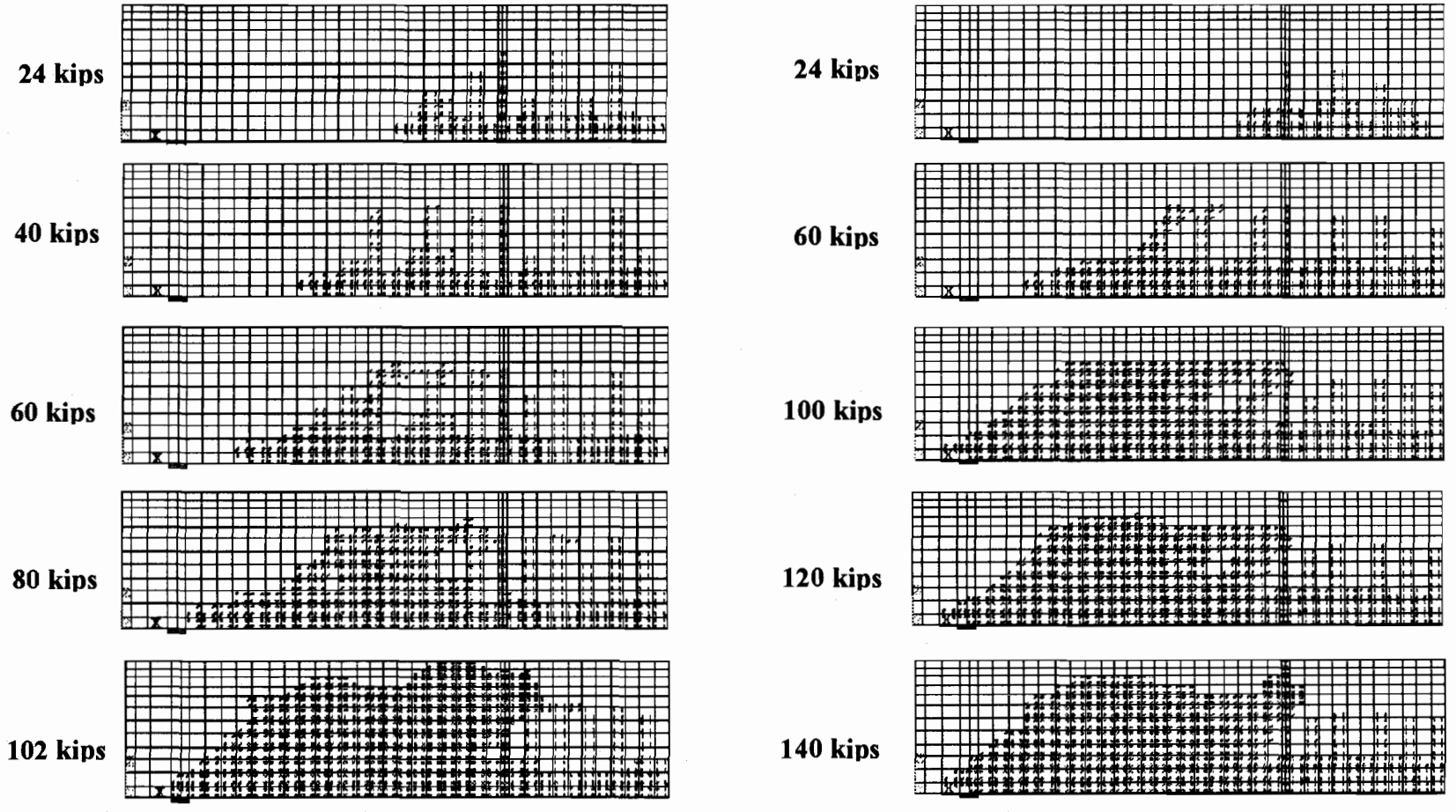

Figure 3.25: Evolution of Crack Patterns: (a) Control Beam; (b) Flexural Strengthened Beam; (c) Shear Strengthened Beam; (d) Flexural/Shear Strengthened Beam

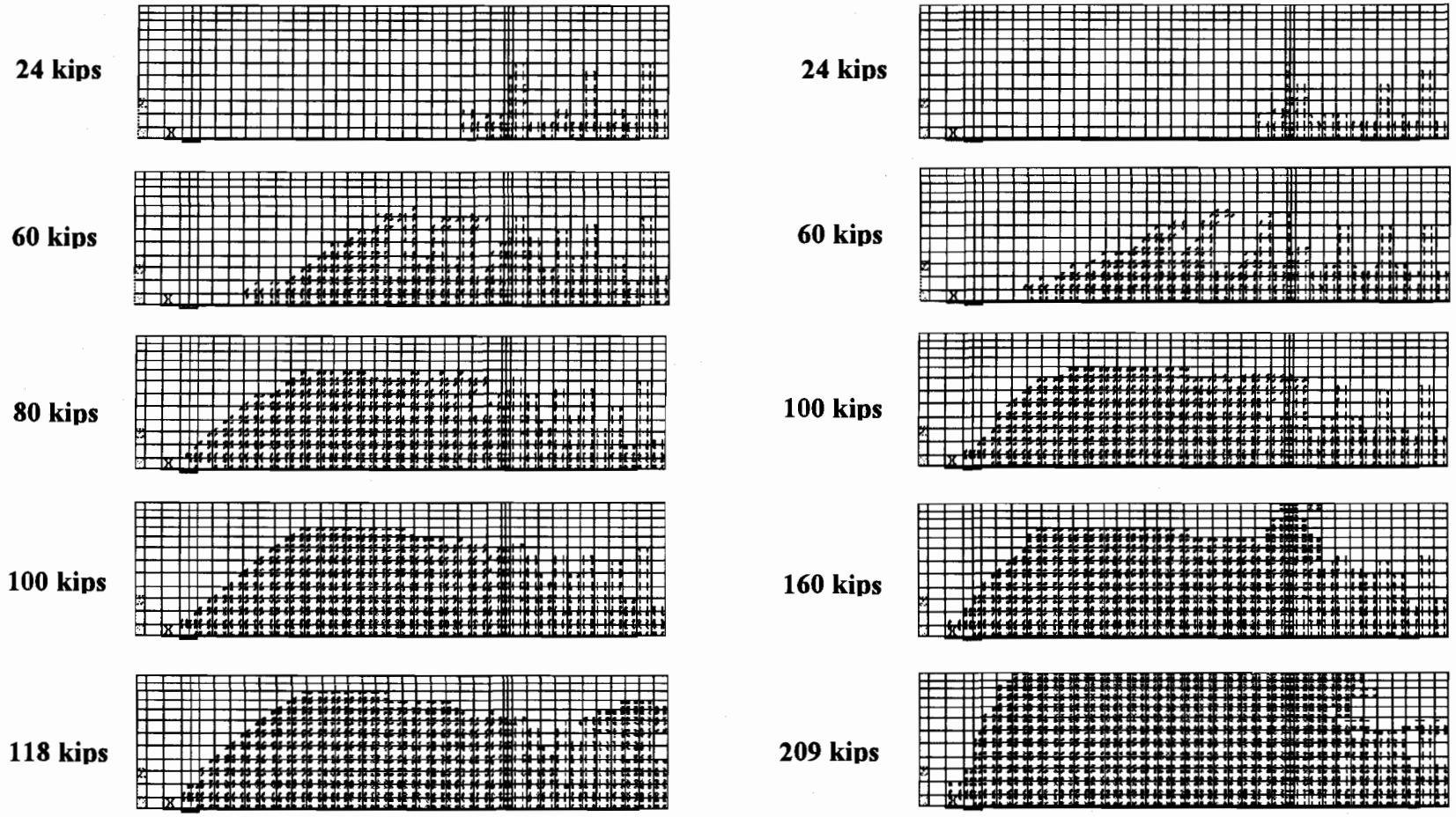

Figure 3.25: (Continued)

3.5. Loads at Failure

All four experimental beams were tested to the maximum achievable load. For the control, flexural strengthened, and shear strengthened beams, the load was the respective beam capacity. However, for the flexural/shear strengthened beam, the maximum load was 160 kips, due to the capacity of the testing machine (McCurry and Kachlakev, 2000).

The ultimate loads for the experimental beams are compared to the final loads from the finite element simulations. As mentioned in Chapter 2, the final loads for all four beams are the last converged load steps from ANSYS, with as small as 1 lb increments. After the final loads, the beam models have very large deflections resulting in unconverged solutions. This is the criterion used to define failure for the four models in this study.

Moreover, the failures of the models are supported by the crack patterns. At the final loads, cracking of the concrete has propagated through the beams from the bottom face to the top face. Table 3.2 shows comparisons between the ultimate loads of the experimental beams and the final loads of the four models from ANSYS.

The ultimate loads of the experimental beams and the final loads from the finite element analyses are compared and show that ANSYS underestimates the strength of the beams by 5%-24%. The comparisons show good agreement between the experimental data and the finite element results. The final loads from the finite element models were anticipated to be lower than the ultimate loads of the experimental beams. The inclined portions of the steel reinforcement are excluded from the finite element

models, and this could be one of the reasons for the final loads from the finite element analyses to be lower than those from the experimental data.

Table 3.2: Comparisons Between Experimental Ultimate Loads and ANSYS Final Loads

Beam	Ultimate load (kips) from Experimental results*	Final load (kips) from ANSYS	%Difference
Control beam	107	102	-5
Flexural beam	155	140	-10
Shear beam	155	118	-24
Flexural/Shear beam	160**	209	N/A

*(McCurry and Kachlakev, 2000)
**This is not an ultimate load. The testing was limited by the testing machine capacity.

Toughening mechanisms at the crack faces may also slightly extend the failures of the experimental beams before complete collapse. The finite element models do not have these mechanisms. Some of these toughening mechanisms are shown in Figure 3.26 (Shah et al., 1995). The grain bridging process is shown in Figure 3.26(a). Bridging occurs when the crack has advanced beyond an aggregate that continues to transmit stresses across the crack. Figure 3.26(b) shows the interlock between the cracked faces. This causes energy dissipation and load transfer through friction and some bridging across the crack. Figure 3.26(c) shows the crack tip blunted by voids. Additional energy is required to propagate the crack with a new blunt tip. Another process is called crack branching as shown in Figure 3.26(d). The crack may propagate

into several braches due to heterogeneity of the concrete. More energy is consumed to form new crack branches.

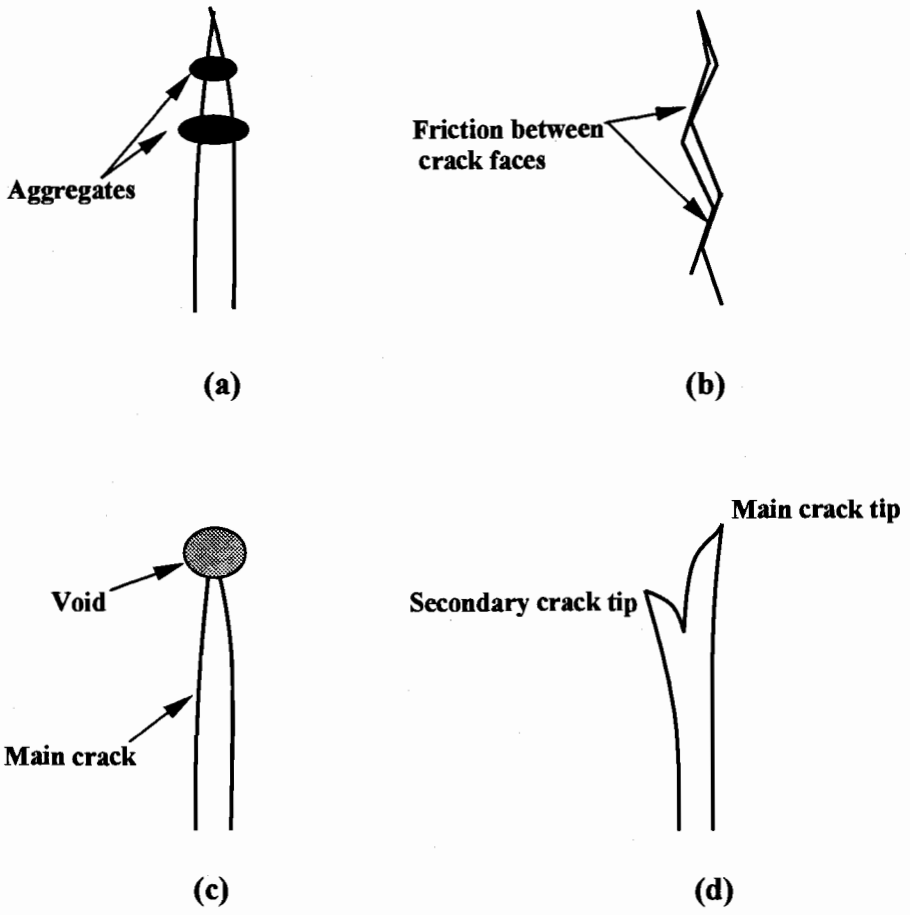

Figure 3.26: Toughening Mechanisms: (a) Aggregate Bridging; (b) Crack-Face Friction; (c) Crack Tip Blunted by Void; (d) Crack Branching (Shah et al., 1995)

Finally, the material properties assumed in this study may be imperfect. The stress-strain curve for the steel used for the finite element beam models should be obtained directly from material testing. The actual reinforcing steel has a different

stress-strain curve when compared to the idealized steel used for the finite element modeling as shown in Figure 3.27. Therefore, this may help to produce the higher ultimate load in the experimental beams. Moreover, the perfectly plastic stress-strain relationship assumed for the concrete after the ultimate compressive stress might also cause the lower failure load in the finite element models.

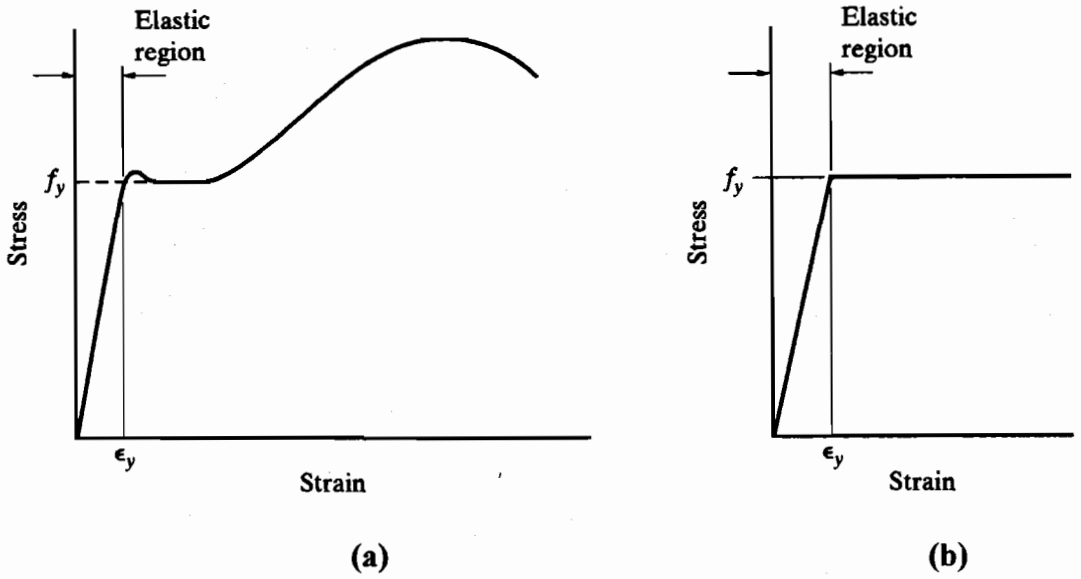

Figure 3.27: Stress-Strain Curve for Reinforcing Steel: (a) As Determined by Tension Test; (b) Idealized (Spiegel and Limbrunner, 1998)

3.6. Crack Patterns at Failure

In the experiment, the failure modes for the four beams were as predicted. The control and flexural strengthened beams failed in shear as anticipated. The shear strengthened beam failed in flexure at the midspan, with yielding of the steel reinforcing followed by a compression failure at the top of the beam. The

flexural/shear strengthened beam was loaded up to the maximum load of 160 kips that the testing machine was able to apply.

Crack patterns obtained from the finite element analyses at the last converged load steps are presented and compared to failure photographs from the experimental beams (Figure 3.28). Note that a photograph at failure of the flexural/shear strengthened beam is not available. Figure 3.28(a) shows a comparison of crack patterns at failure from the finite element analysis and the experimental results for the control beam. The crack pattern from ANSYS and the photograph of the experimental beam agree very well. For the finite element model, smeared cracks spread over the high shear stress region and occur mostly from the support toward the loading area. Figure 3.28(b) shows that the crack patterns for the flexural strengthened beam from both the finite element analysis and the experiment are similar to those for the control beam. The ANSYS program accurately predicts that both the control and the flexural strengthened beam fail in shear, but the flexural strengthened beam fails at a higher load.

Figure 3.28(c) shows good agreement between the crack pattern from ANSYS and the photograph of the experimental shear strengthened beam. Numerous cracks occur at midspan of the finite element model rather than underneath the loading location. The crack pattern and steel yielding at the midspan (Figure 3.4) for the finite element shear strengthened beam support the experimental results that the beam fails in flexure.

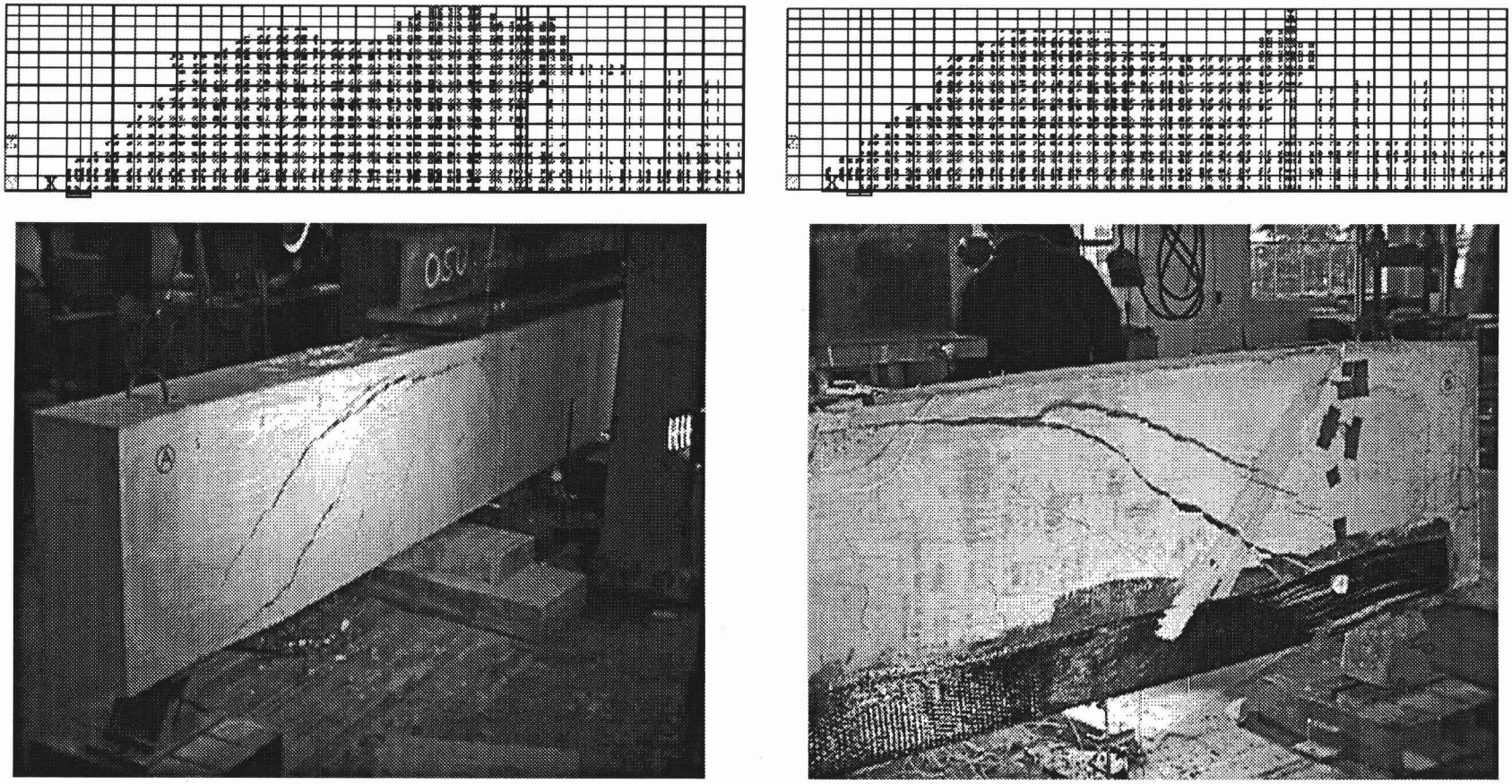

(a) (b)

Figure 3.28: Crack Patterns at Failure: (a) Control Beam; (b) Flexural Strengthened Beam; (c) Shear Strengthened Beam; (d) Flexural/Shear Strengthened Beam

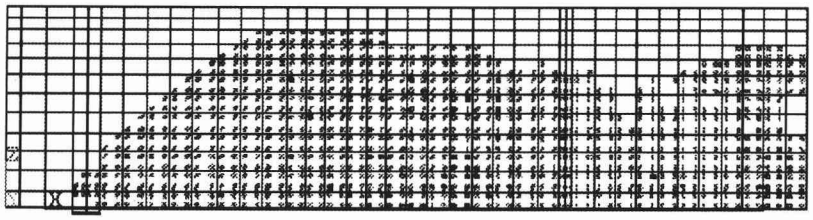

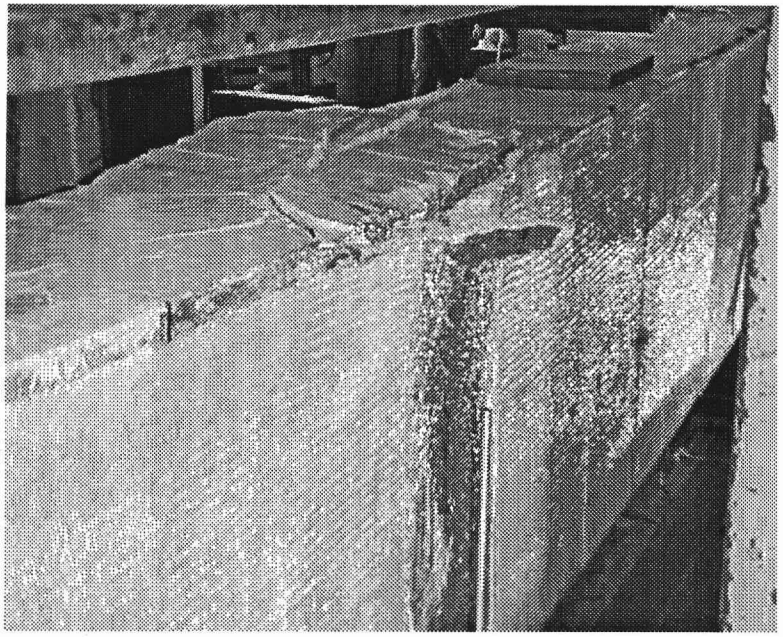

(c)

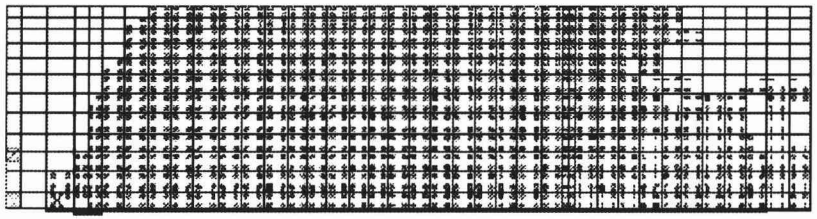

Photo N/A
Beam did not fail.

(d)

Figure 3.28: (Continued)

Calculations suggested that the experimental flexural/shear strengthened beam would be limited by the crushing strength of the concrete and fail in flexure (McCurry and Kachlakev, 2000). Figure 3.28(d) illustrates the final crack pattern for the flexural/shear strengthened beam predicted by the ANSYS program. Numerous compressive cracks occur at the top part of the beam, and many flexural cracks are observed at midspan as well. Moreover, the steel at the midspan in the model yields as shown in Figure 3.5. These observations support the conclusion that the beam would fail in flexure.

3.7. Stress Contours in Concrete

Figure 3.29 shows stress contours in the concrete for the finite element beam models. For each model, stress contours are shown at three different applied load steps; at 15 kips (uncracked concrete), 50 kips (cracked concrete), and at the last load step for each beam. Note that the time step (TIME) indicated in each plot represents the applied load to the model, in which the units are lbs. The direction of the stresses (SX) is in the x direction (along the length of the beams). The units for stress in each plot are lb/in^2. Negative values are compressive stresses, whereas positive values are tensile stresses.

As shown in the figure, the stress contours from the ANSYS program can effectively display stresses that develop in the concrete for each model. After cracking of the concrete, cracked concrete elements in the models result in discontinuities in the stress contours.

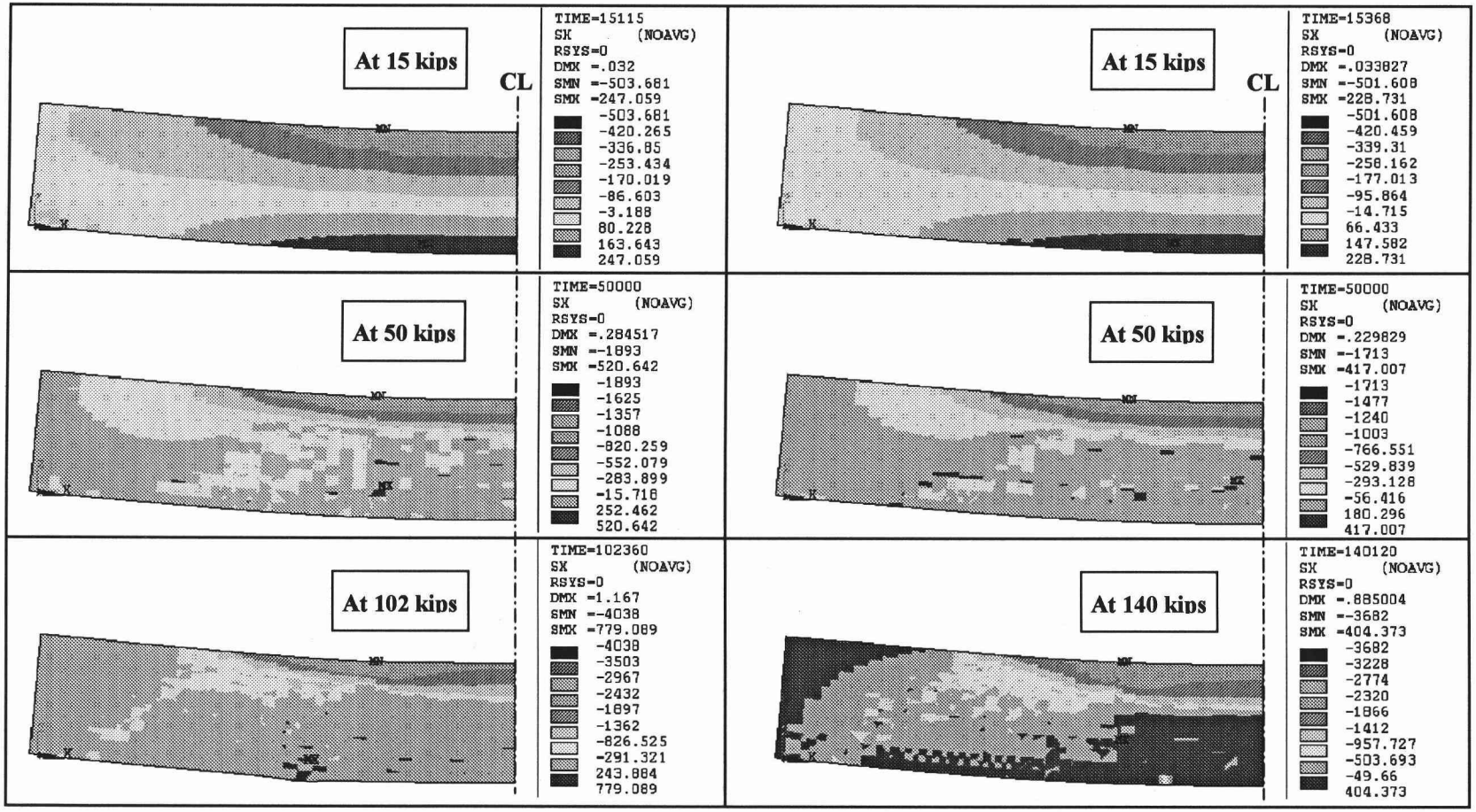

(a) (b)

Figure 3.29: Stress Contours in Concrete: (a) Control Beam; (b) Flexural Strengthened Beam; (c) Shear Strengthened Beam; (d) Flexural/Shear Strengthened Beam

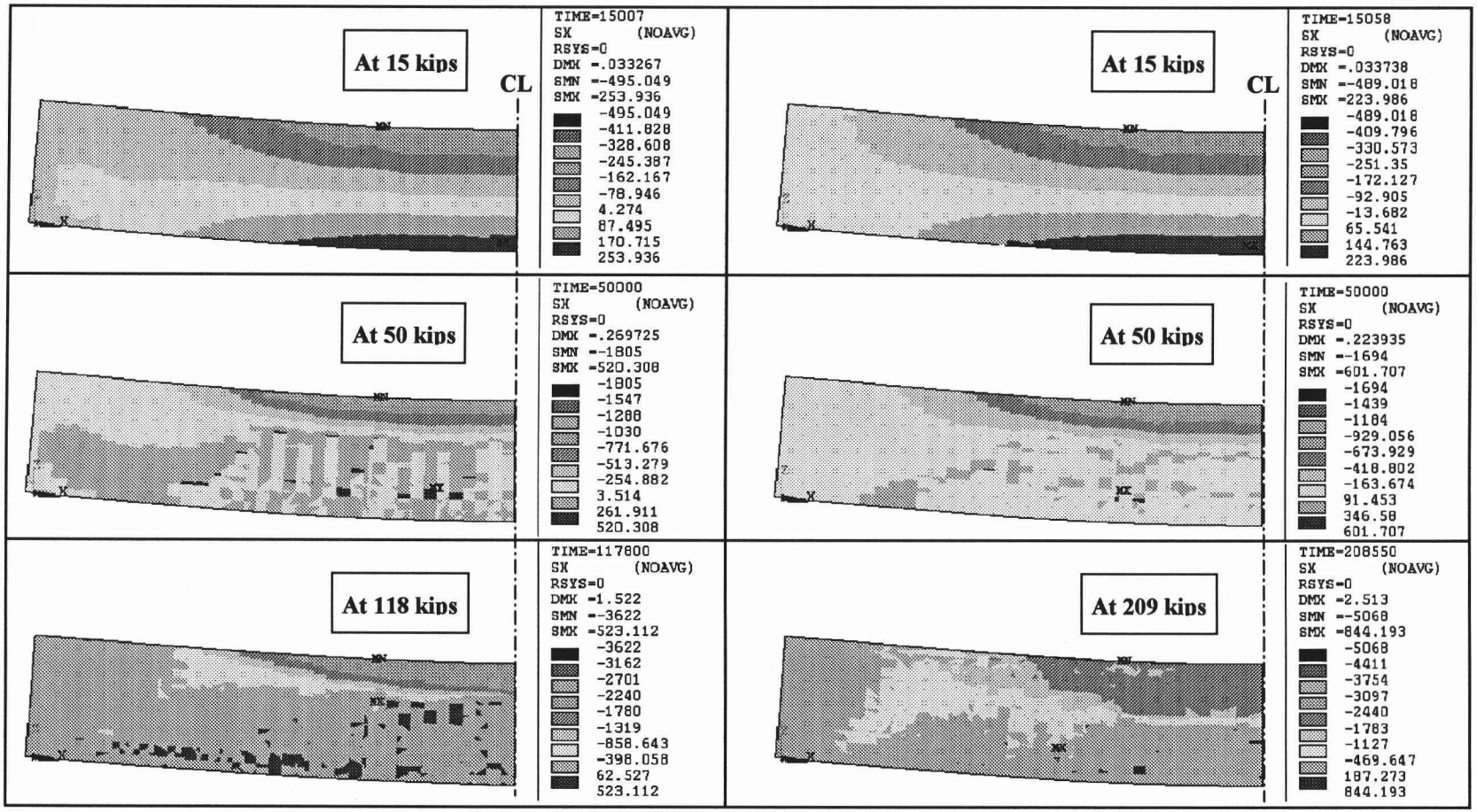

(c) **(d)**

Figure 3.29: (Continued)

3.8. Maximum Stresses in FRP Composites

For the experimental flexural and shear strengthened beams, there was no evidence that the FRP reinforcing failed before overall failure of the beams. The finite element analyses provide stresses occurring at the integration points of FRP layered solid elements. Maximum stresses are obtained at the last converged load step. Table 3.3 shows a summary of the maximum tensile stresses occurring in the FRP composites for the FRP strengthened beams and the ultimate tensile strength of the FRP composites. Figure 3.30 shows locations of the maximum stresses in the FRP composites for the FRP strengthened beams.

Table 3.3: Summary of Maximum Stresses and Ultimate Tensile Strengths of FRP Composites

Beam	Maximum tensile stress (ksi)	Ultimate tensile strength (ksi)*	Location (x, y, z) (in.)**
Flexural beam (CFRP)	28.7	139	(66,6,0)
Shear beam (GFRP)	7.22	87.0	(114,4,0)
Flexural/Shear beam	71.8 (CFRP) 5.91 (GFRP)	139 (CFRP) 87.0 (GFRP)	(120,0,0) (57,4,0)

* (Kachlakev and McCurry, 2000)
** (x, y, z) corresponds to (length, width, height) directions on the beams, and the origin (0, 0, 0) is at a corner of the bottom face of the beams as shown in Figure 3.30(a).

Table 3.3 supports the experimental observations that the CFRP and GFRP on the flexural and shear strengthened beams do not rupture before the overall failures of the beams. The tensile stress (at the last converged load step) in the CFRP for the

flexural/shear strengthened model at midspan represents the maximum stress developed in the composite laminate. Nonetheless, the stress is substantially less than the ultimate tensile strength.

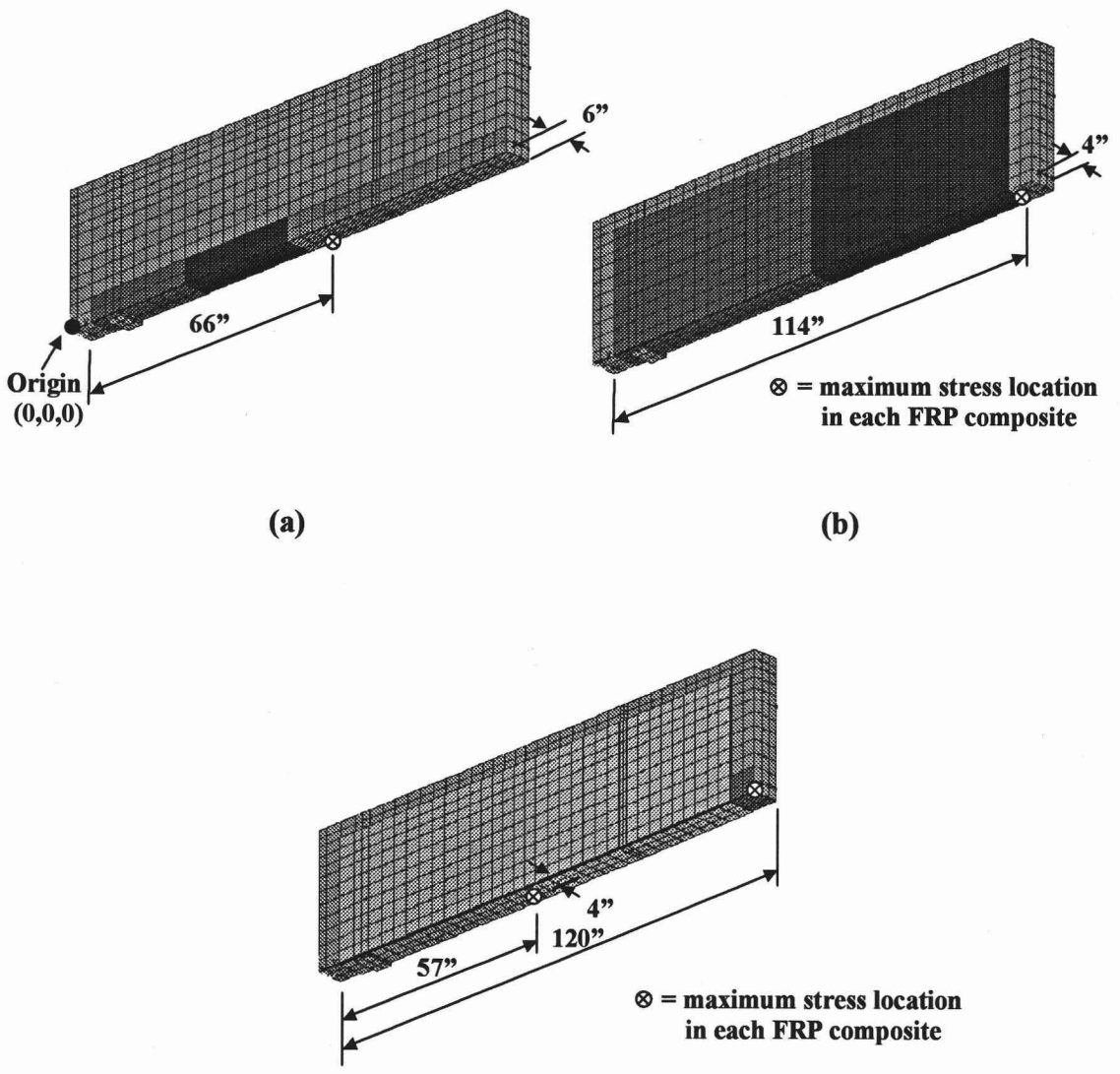

Figure 3.30: Locations of Maximum Stresses in FRP Composites for FRP Strengthened Beams: (a) Flexural Strengthened Beam; (b) Shear Strengthened Beam; (c) Flexural/Shear Strengthened Beam

3.9. Comparisons to Parallel Research

A parallel research effort was accomplished at Oregon State University by Chansawat (2000). Only two full-scale beams, i.e., the control beam and the flexural/shear strengthened beam, were modeled also using the ANSYS finite element program by Chansawat (2000).

The control beam models from this study and Chansawat (2000) have nearly the same geometric configurations. However, one difference between the two control beam models was the method of mesh generation. This study uses mesh generation based on a solid modeling method, whereas the mesh generation of Chansawat's model was based on a direct generation method. The load stepping defined for the analyses was also different, especially the load step sizes close to failure. Chansawat used 0.1 lb as the minimum load step size, whereas this study used a 1 lb load increment.

The flexural/shear strengthened beams from the two studies also have nearly the same geometric configurations as for the control beam except for the number of elements due to the different methods used in modeling the FRP composites. For Chansawat's model, CFRP and GFRP composites were modeled as layers in one element, whereas for this study each FRP composite is separately modeled. Mesh generation and load stepping for the two studies are also different as for the control beam.

Comparisons of the results from both studies showed that the stiffnesses of the models are almost identical for both the control and flexural/shear strengthened beam models. The crack patterns predicted by the ANSYS program from the two studies are very similar. However, the load-carrying capacities of the models from the two studies

are slightly different. The control beam modeled by Chansawat has a failure load higher than the model from this study by 0.5%, and the failure load of the flexural/shear strengthened beam modeled by Chansawat is higher than that from this study by 4%. The differences in the FRP composite modeling and the load stepping between the two analyses could cause these differences in the load-carrying capacities.

4. CONCLUSIONS AND RECOMMENDATIONS

4.1. Conclusions

1. The finite element method using the ANSYS program can effectively simulate the general behavior of reinforced concrete beams both before and after applying FRP composites from the linear through nonlinear ranges and up to failure.

2. The general behaviors of the finite element models represented by the load-deflection plots at midspan show good agreement with the experimental data provided from the full-scale beam tests.

3. The load-deflection plots resulting from the finite element models show that the finite element models are stiffer than the experimental beams in the linear range by 12%-66%. The first cracking loads for all four beams calculated by the finite element program are higher than those from the experimental data by 6%-34%. After first cracking of the concrete, overall stiffness of the finite element models is slightly higher than the experimental beams by 14%-28%. The finite element models do not account for microcracks occurring in the actual concrete; therefore, the finite element models are stiffer than the experimental beams; and the effect of bond slip between the concrete and steel reinforcing is not included in the finite element models (perfect bond is assumed in the finite element analyses) and this also results in the stiffness of the finite element models being higher than that for the experimental beams.

4. The load-strain plots showing local behavior at selected locations from the finite element analysis show fair agreement to those from the experimental data.

5. The final loads from the finite element analyses are lower than the ultimate loads from the experimental results by 5%-24%, in part because inclined portions of the steel reinforcement are not included; the effects of concrete toughening mechanisms are ignored in the models; and the material properties assumed in the models may be imperfect.

6. The load carrying capacity of the flexural/shear strengthened beam predicted by the finite element analysis is higher than that of the control beam by 105%, which agrees very well with hand calculations showing that the FRP strengthened beam has a higher ultimate load than the control beam by 104%.

7. The crack patterns at the final loads from the finite element models correspond well with the failure modes of the experimental beams, and the crack pattern predicted by the finite element analysis for the flexural/strengthened beam agrees with the hand calculations showing that the beam fails in flexure.

4.2. Recommendations for Modeling of FRP-Strengthened Reinforced Concrete Beams

1. A stress-strain curve for the steel reinforcement obtained from material testing may be used in the finite element modeling to obtain improved results.

2. Improvement in concrete modeling may be made by adding a descending portion (strain softening) to the concrete stress-strain curve.

3. Taking advantage of the symmetry of structures reduces computational time and computer disk space requirements, however boundary conditions must be properly defined.

4. Modeling the bond slip behavior between the steel reinforcement and the concrete may improve results.

5. For the beam tests, a steel plate with a line support was needed at the support locations. The steel plate provides a more even stress distribution over the support area to avoid problems of stress concentration, and the line support allows rotation of the steel plate to prevent excessive cracking of concrete elements at the support location.

6. A convergence study must be carried out to determine an adequate number of elements for the models.

7. For nonlinear analysis of a reinforced concrete beam, the total load applied to a model must be divided into a number of load steps. Sufficiently small load step sizes are required particularly at changes in behavior of the reinforced concrete beam, i.e. major cracking of concrete, yielding of steel, and approaching failure of the reinforced concrete beam. Properly defining minimum and maximum sizes for each load step depending upon the behavior of the reinforced concrete beam assists in convergence of the solutions and reduces computer computational time.

BIBLIOGRAPHY

ACI 318-99, American Concrete Institute, Building Code Requirements for Reinforced Concrete, American Concrete Institute, Farmington Hills, Michigan, 1999.

ACI 440, American Concrete Institute, Guide for the Design and Construction of Externally Bonded FRP Systems for Strengthening Concrete Structures, American Concrete Institute, Farmington Hills, Michigan, 2000.

Adams, V. and Askenazi, A., *Building Better Products with Finite Element Analysis*, OnWord Press, Santa Fe, New Mexico, 1998.

American Society for Testing and Materials (ASTM) Subcommittee C09.64, *Standard Test Method for Pulse Velocity Through Concrete*, Designation C 597-83, ASTM, West Conshohocken, Pennsylvania, 1983.

American Society for Testing and Materials (ASTM) Subcommittee C09.70, *Standard Test Method for Static Modulus of Elasticity and Poisson's Ratio of Concrete in Compression*, Designation C 469-94, ASTM, West Conshohocken, Pennsylvania, 1994.

ANSYS, ANSYS User's Manual Revision 5.5, ANSYS, Inc., Canonsburg, Pennsylvania,1998.

Arduini, M., Di Tommaso, A., and Nanni, A., "Brittle Failure in FRP Plate and Sheet Bonded Beams," ACI Structural Journal, 94(4), pp. 363-370, 1997.

Bangash, M. Y. H., *Concrete and Concrete Structures: Numerical Modeling and Applications*, Elsevier Science Publishers Ltd., London, England, 1989.

Bathe, K. J., *Finite Element Procedures*, Prentice-Hall, Inc., Upper Saddle River, New Jersey, 1996.

Chansawat, K., "Nonlinear Finite Element Analysis of Reinforced Concrete Structures Strengthened With FRP Laminates," personal communication, Corvallis, Oregon, 2000.

Chen, A. C. T. and Chen, W. F., "Constitutive Relations for Concrete," Journal of the Engineering Mechanics Division, ASCE, Vol. 101, No. EM4, pp. 465-481, August 1975.

CH2M HILL, Inc., Consulting Engineers-in conjunction with TAMS Consultants, "Evaluation and Resolution of Under Capacity State Bridges: Bridge#04543, Horsetail Creek Bridge, Corvallis, Oregon, June 1997.

Desayi, P. and Krishnan, S., "Equation for the Stress-Strain Curve of Concrete," Journal of the American Concrete Inst., 61, pp. 345-350, March 1964.

Gere, J. M. and Timoshenko, S. P., *Mechanics of Materials*, PWS Publishing Company, Boston, Massachusetts, 1997.

Gibson, R. F., *Principles of Composite Material Mechanics*, McGraw-Hill, Inc., New York, New York, 1994.

Hemmaty, Y., "Modelling of the Shear Force Transferred Between Cracks in Reinforced and Fibre Reinforced Concrete Structures," Proceedings of the ANSYS Conference, Vol. 1, Pittsburgh, Pennsylvania, August 1998.

Hemmaty, Y., DeRoeck, G., and Vandewalle, L., "Parametric Study of RC Corner Joints Subjected to Positive Bending Moment by Nonlinear FE Model," Proceedings of the ANSYS Conference, Vol. 2, Pittsburgh, Pennsylvania, June 1992.

Huyse, L., Hemmaty, Y., and Vandewalle, L., "Finite Element Modeling of Fiber Reinforced Concrete Beams," Proceedings of the ANSYS Conference, Vol. 2, Pittsburgh, Pennsylvania, May 1994.

Hyer, M.W., *Stress Analysis of Fiber-Reinforced Composite Materials*, WCB/McGraw-Hill, Inc., Boston, Massachusetts, 1998.

Isenburg, J. (editor), "Finite Element Analysis of Reinforced Concrete Structures II," ASCE, New York, New York, 1993.

Kachlakev, D. I., "Strengthening Bridges Using Composite Materials," *FHWA Report No. OR-RD-98-08*, Corvallis, Oregon, 1998.

Kachlakev, D.I. and McCurry, D., Jr., "Simulated Full Scale Testing of Reinforced Concrete Beams Strengthened with FRP Composites: Experimental Results and Design Model Verification," United States Department of Transportation, Federal Highway Administration and Oregon DOT, Salem, Oregon, June 2000.

Kachlakev, D. I., Miller, T. H., Yim, S., Chansawat, K., and Potisuk, T., "Linear and Nonlinear Finite Element Modeling of Reinforced Concrete Structures Strengthened With FRP Laminates," United States Department of Transportation, Federal Highway Administration and Oregon DOT, Salem, Oregon, August 2000.

Kaw, A. K., *Mechanics of Composite Materials*, CRC Press LLC, Boca Raton, Florida, 1997.

Lin, C. and Scordelis, A. C., "Nonlinear Analysis of RC Shells of General Form," Journal of the Structural Division, ASCE, 101(ST3), pp. 523-538, March 1975.

Logan, D. L., *A First Course in the Finite Element Method*, PWS Publishing Company, Boston, Massachusetts, 1992.

Marshall, O. S. and Busel, J. P., "Composite Repair/Upgrade of Concrete Structures," 4th Materials Conference, "Materials for the New Millennium", editor K. Chong, American Society of Civil Engineers, Washington, D. C., November 1996.

McCurry, D., Jr. and Kachlakev, D. I., "Strengthening of Full Sized Reinforced Concrete Beam Using FRP Laminates and Monitoring with Fiber Optic Strain Gauges," in "Innovative Systems for Seismic Repair and Rehabilitation of Structures," Design and Applications, Technomic Publishing Co., Inc., Philadelphia, Pennsylvania, March 2000.

Mindess, S. and Young, J. F., *Concrete*, Prentice-Hall, Inc., Englewood Cliffs, New Jersey, 1981.

Neville, A. M., *Properties of Concrete*, John Wiley & Sons, Inc., New York, New York, 1996.

Ngo, D. and Scordelis, A. C., "Finite Element Analysis of Reinforced Concrete Beams," Journal of the American Concrete Inst., 64(3), pp. 152-163, 1967.

Nilson, A. H., "Nonlinear Analysis of Reinforced Concrete by the Finite Element Method," Journal of the American Concrete Inst., 65(9), pp. 757-766, 1968.

Nilson, A. H., *Design of Concrete Structures*, McGraw-Hill, Inc., New York, New York, 1997.

Patnaik, A. K., "Horizontal Shear Strength of Composite Concrete Beams With a Rough Interface," Ph.D. Dissertation, Department of Civil Engineering, University of Calgary, Calgary, Alberta, Canada, December 1992.

Rashid, Y. R., "Ultimate Strength Analysis of Prestressed Concrete Pressure Vessels," Nuclear Engineering and Design, 7(4), pp. 334-344, Amsterdam, Netherlands, April 1968.

Seible, F., Hegemier, G., and Karbhari, V., "Advanced Composite for Bridge Infrastructure Renewal," 4th International Bridge Engineering Conference, Proceedings, Vol. 1, San Francisco, California, August 29-30 1995.

Shah, S. P., Swartz, S. E., and Ouyang, C., *Fracture Mechanics of Concrete*, John Wiley & Sons, Inc., New York, New York, 1995.

Spiegel, L. and Limbrunner, G. F., *Reinforced Concrete Design*, Prentice-Hall, Inc., Upper Saddle River, New Jersey, 1998.

Steiner, W., "Strengthening of Structures with CFRP Strips," Advanced Composite Materials for Bridges and Structures, 2nd International Conference, Proceedings, editor M.El-Bardry, Montreal, Canada, August 1996.

Suidan, M. and Schnobrich, W. C., "Finite Element Analysis of Reinforced Concrete," Journal of the Structural Division, ASCE, ST10, pp. 2109-2122, October 1973.

Tedesco, J. W., Stallings J. M., and El-Mihilmy, M., "Finite Element Method Analysis of a Concrete Bridge Repaired with Fiber Reinforced Plastic Laminates," Computers and Structures, 72, 379-407, 1999.

Tedesco, J. W., Stallings J. M., El-Mihilmy, M., and McCauley, M., "Rehabilitation of Concrete Bridges Using FRP Laminates," 4th Materials Conference, "Materials for the New Millennium", editor K. Chong, American Society of Civil Engineers, Washington, D. C., November 1996.

Ugural, A. C. and Fenster, S. K., *Advanced Strength and Applied Elasticity*, Prentice-Hall Inc., Upper Saddle River, New Jersey, 1995.

Vecchio, F. J. and Bucci, F., "Analysis of Repaired Reinforced Concrete Structures," Journal of the Structural Division, ASCE, 125(6), 644-652, June 1999.

William, K. J. and Warnke, E. P., "Constitutive Model for the Triaxial Behavior of Concrete," Proceedings, International Association for Bridge and Structural Engineering, Vol. 19, ISMES, Bergamo, Italy, pp. 174, 1975.